The University of Queensland
Australia
CREATE CHANGE

# SMP Poster Day 2021
# Abstract Booklet

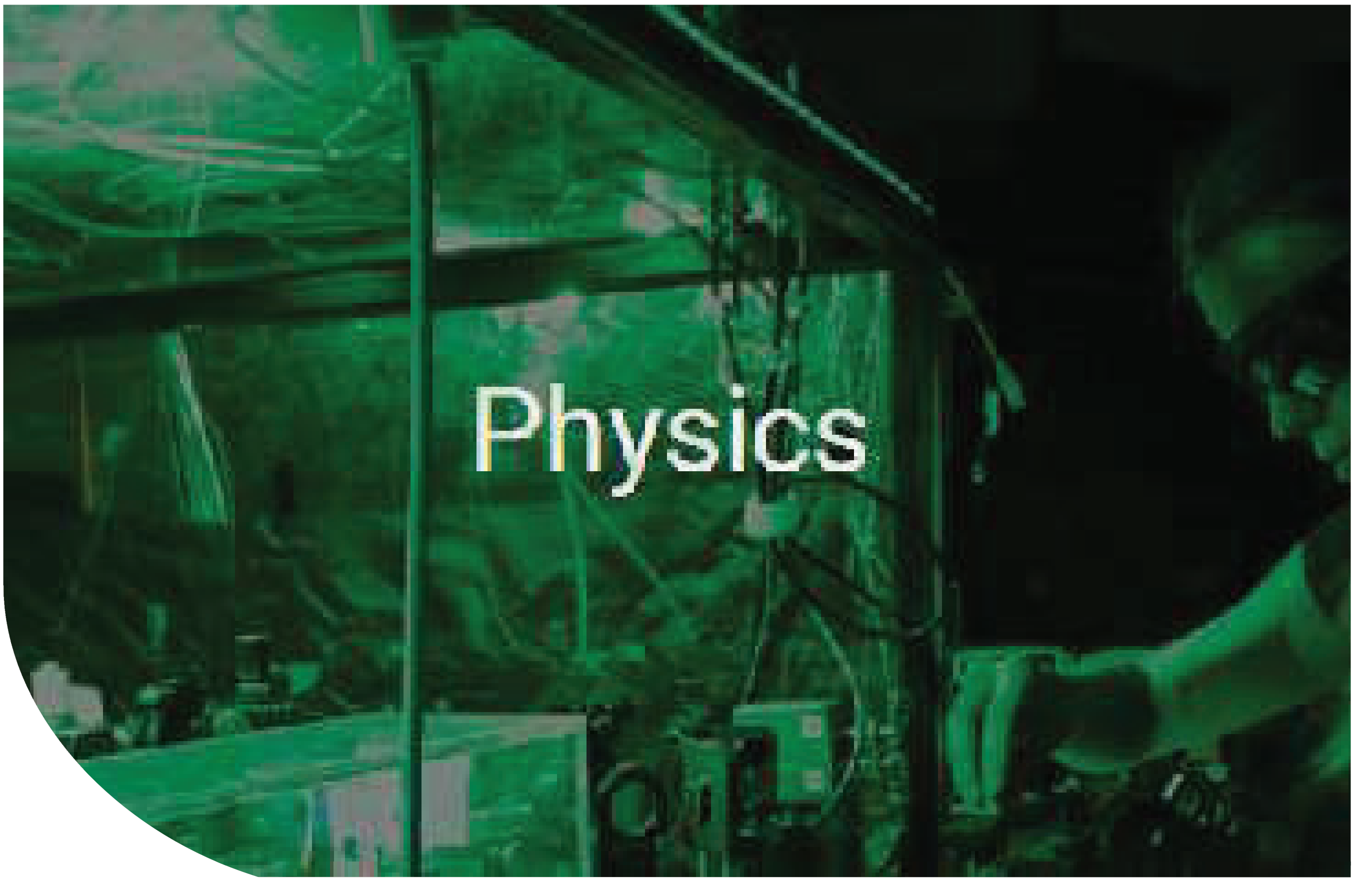
Physics

# Effective Field Theories of Large Scale Structure (and where to find them)

Aaron Glanville  Cullan Howlett  Tamara Davis

*University of Queensland*

The University of Queensland
Australia

## Cosmic Confusion

Improvements in the accuracy of our cosmological constraints have exposed **clear inconsistencies between datasets**- Understanding what is driving these inconsistencies has become a pressing challenge

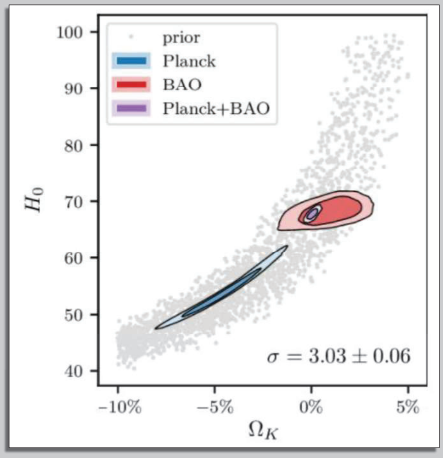


Recent attention has been drawn to curvature constraints derived from cosmic microwave background (CMB) measurements- While CMB+late universe fits strongly prefer flatness, fits to the CMB alone prefer curvature to 3$\sigma$. This **inconsistency raises questions over the robustness of joint $\Omega_K$ constraints [1]**

## EFTofLSS- A New Perspective?

Effective Field Theories of Large Scale Structure (**EFTofLSS**) have show promise at constraining cosmology independently of CMB measurements. EFTofLSS models the entire power spectrum (up to semi non-linear modes) using physically motivated perturbations of the linear spectrum. These **small scale modes encode a vast amount of clustering information**, with minimal cosmological assumptions

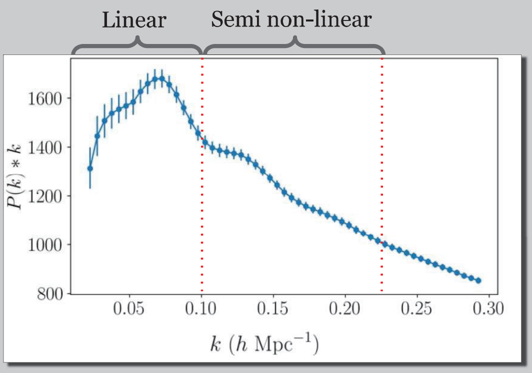


Using full shape information, Chudaykin et. al 2020 recover a mildly curved universe with a <1$\sigma$ significance, independently of any CMB information [2]. Importantly, while independent of the CMB, **EFT fits of $\Omega_K$ have so far relied on reconstruction techniques which assume flatness** to improve SNR.

## Our Work

### "What perspective does the full-shape of the galaxy power spectrum provide on the curvature tension?"

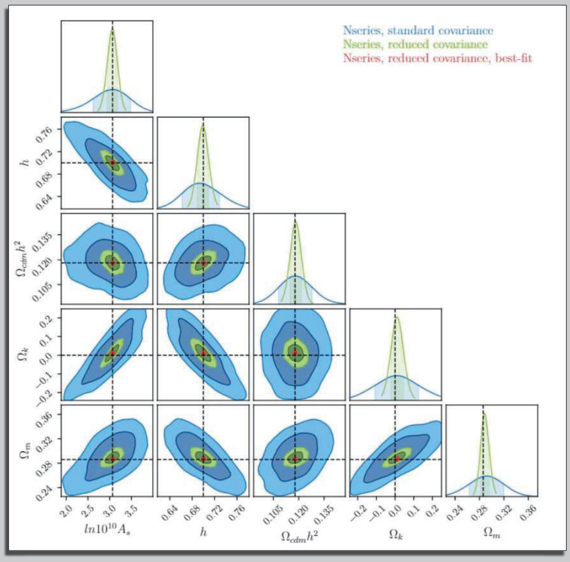


We disentangle full-shape clustering information by fitting the pre-reconstruction power spectrum, with **minimal external assumptions or priors**

We develop a publicly available pipeline to **effortlessly combine clustering measurements**, across both flat and curved cosmological models

Tests of our implementation on high resolution N-body mock catalogues provide **remarkably accurate constraints**, across curved and flat models

We use our pipeline to combine measurements from every major clustering survey (6dF + BOSS + eBOSS), in the **most comprehensive full-shape analysis to date**.

Full-shape only constraints without the assumption of reconstruction **increase the preference for curvature from 1$\sigma$ to 2$\sigma$**. Interestingly, our best-fit is skewed to a milder curvature, consistent with the literature

Posterior distribution highlights the presence of **significant model degeneracies**, even with our comprehensive clustering sample

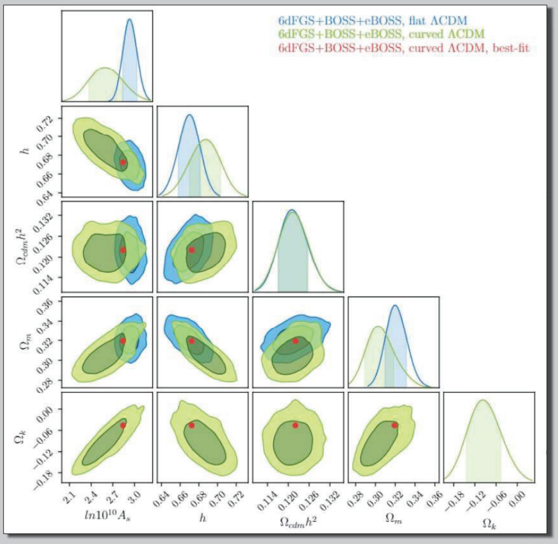


## Conclusions

**EFTofLSS offers a remarkable alternative perspective to investigate tensions between major datasets in the literature. We fit the most comprehensive set of full shape measurements to date, generating robust constraints of curvature. Importantly, these constraints do not rely on external information, offering a powerful tool to disentangle our cosmological models and assumptions. Our publicly available code supports the effortless combination of clustering measurements, allowing for easy integration with future results**

## Bibliography:

[1] Handley 2019 (arxiv: 1908.09139)
[2] Chudaykin et. al 2020 (arxiv: 2009.10106)

**Title:** Effective Field Theories of Large Scale Structure (and where to find them)

**Candidate:** Aaron Glanville

**Abstract:**

Remarkable improvements in our constraining power have exposed inconsistencies between cosmological datasets. We use recent advances in modelling the full shape of the galaxy power spectrum to provide a new perspective on these emerging tensions. Using the most comprehensive range of clustering measurements to date, we robustly constrain spatial curvature with minimal model assumptions or priors, recovering a ~2 \sigma preference for curvature. Our results bring into question the internal consistency of constraints derived from clustering measurements which use reconstruction algorithms (which assume flatness)

# Relativistic quantum particles with *real* trajectories

J. Foo, E. Asmodelle, A.P. Lund, T.C. Ralph
CQC2T

## 'Standard' quantum mechanics:

- Indeterministic: Born rule, $|\psi(x,t)|^2$
- $\psi(x,t)$–collapse: 'measurement problem'
- Nonlocal: EPR correlations

## Bohmian mechanics:

- Deterministic: $\psi(x,t)$ is a hidden variable
- Realistic: no measurement problem
- Nonlocal: $\psi(x,t)$ is a pilot wave

## Aims:

- Reformulate Bohmian mechanics to include relativistic regimes
- Connect photon trajectories to an operational measurement formalism

## Setup:

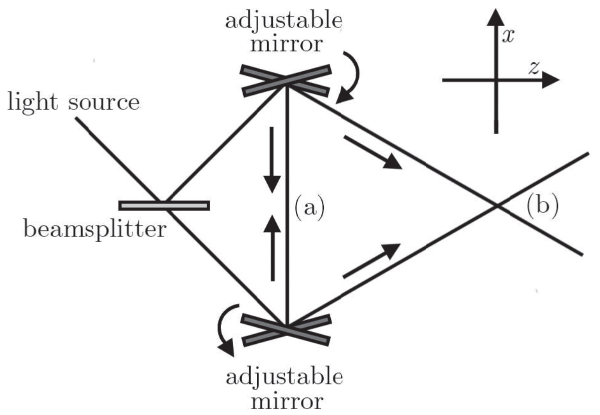


(a) 'Headon collision', (b) 'grazing collision'

*Bohmian*

*weak*

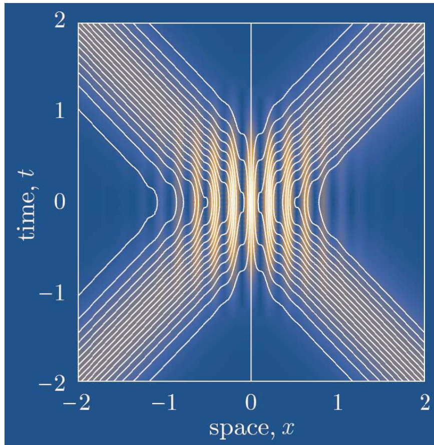


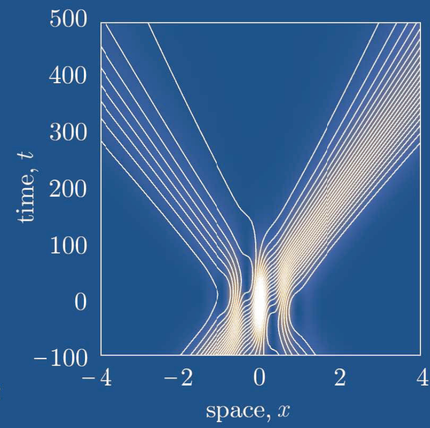


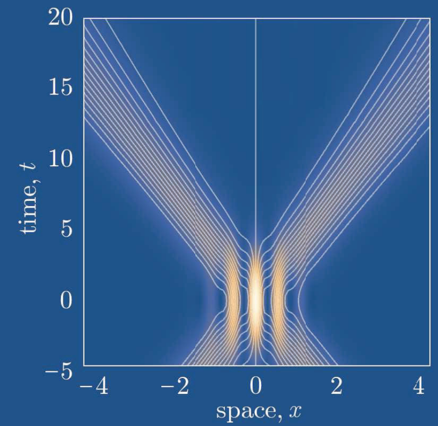


hoton

*theory?*

nload the

## Theory:

- Weak measurement (WM): weakly measure observable $\hat{a}$ from an $N$-particle ensemble to extract $\langle \hat{a} \rangle$ with arbitrarily high precision
- Weak value: WM of $\hat{a}$ conditioned on a later projective measurement:

$$\langle \hat{a}_w \rangle = \mathrm{Re}\frac{\langle \phi | \hat{a} | \psi \rangle}{\langle \phi | \psi \rangle}$$

- Relativistic velocity field:

$$V(x,t) = \frac{p_x}{E} \Rightarrow \frac{\mathrm{Re}\langle x | \hat{p}_x | \psi \rangle}{\mathrm{Re}\langle x | \hat{H} | \psi \rangle}$$

WMs of $\hat{p}$, $\hat{H}$ conditioned on $|x\rangle$. Express in terms of Klein-Gordon conserved current:

$$V(x,t) = \frac{\mathrm{Im}\ \psi^*(x,t)\partial^x\psi(x,t)}{\mathrm{m}\ \psi^*(x,t)\partial^t\psi(x,t)} = \frac{j(x,t)}{\rho(x,t)}$$

## The photon (time-travelling) metric:

- Pilot wave $\Rightarrow$ Bohmian metric

$$ds^2 = -(1-v_s^2)dt^2 - 2v_s dx dt + dx^2$$

where $v_s = \big(V(x,t)-1\big)\mathrm{sgn}\big(V(x,t)\big)$.

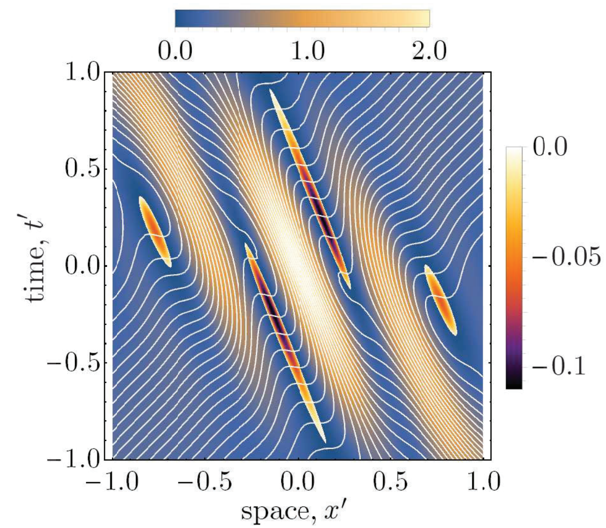

**Title:** Relativistic Bohmian trajectories of photons

**Candidate:** Joshua Foo

**Abstract:**

Bohmian mechanics is a nonlocal hidden-variable interpretation of quantum theory which predicts that particles follow deterministic trajectories in spacetime. Historically, the study of Bohmian trajectories has been restricted to non relativistic regimes due to the widely held belief that the theory is incompatible with special relativity. Here we derive expressions for the relativistic velocity and spacetime trajectories of photons in a Michelson-Sagnac-type interferometer. The trajectories satisfy quantum-mechanical continuity and the relativistic velocity addition rule. Our new velocity equation can be operationally defined in terms of weak measurements of momentum and energy. We finally propose a modified Alcubierre metric which could give rise to these trajectories within the paradigm of general relativity.

# Chiral quantum state transfer in waveguide QED

**Pradeep Nandakumar**[1], Prasanna Pakkiam[1], Mikhail Pletyukhov[2]
Arkady Fedorov[1]

[1]*ARC Centre of Excellence for Engineered Quantum Systems,*
*The University of Queensland, St Lucia, Queensland 4072, Australia*
[2]*RWTH Aachen University, Aachen, Germany*

## Abstract

Coherent transfer of information between qubits is fundamental to achieving any quantum information processing task. Here we discuss experimental progress towards developing a tunable chiral quantum system that allows us to select the direction in which the quantum information is shared between qubits. The directional qubit-qubit interaction is achieved via photonic bound states that live in a waveguide composed of an array of coupled cavities. The bound state is induced in the bandgap by suitably engineering the tunnel couplings and on-site potentials of the cavities in the array. In-situ control of the chirality of the bound states is achieved by a frequency tunable Transmon qubit coupled to the central site of the waveguide.

## System design

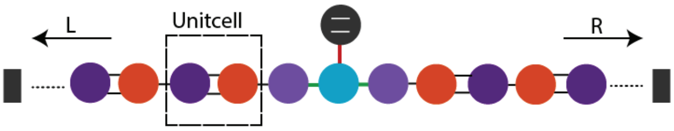


- The waveguide is composed of two chains (L/R) linked through a central site (●). Each site is realized as a LC resonator.
- Both the on-site potential $\pm U_0$ and tunnel couplings $t_1, t_2$ are periodically modulated realising the Rice-Mele model.
- The central site which acts as a defect induces a photonic bound state in the bandgap.
- Coupling qubit to the central site allows us to control the directionality of the bound states

## Directional quantum state transfer

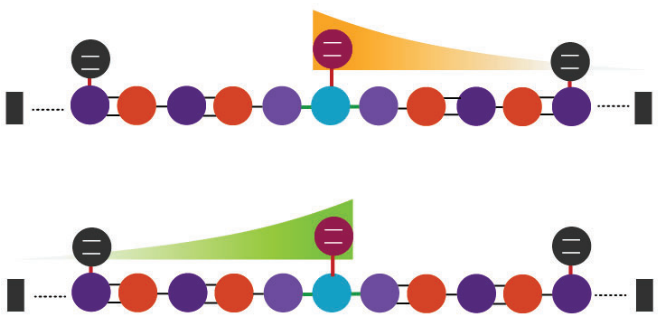

- In the regime where $t_c \gg U_o$ an exponentially localized state lives in the bandgap.

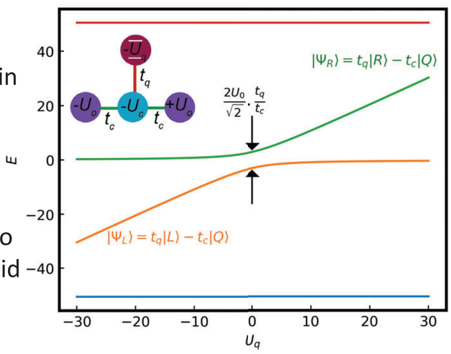


- The chirality of the bound state can be dynamically tuned to $|\Psi_L\rangle$ or $|\Psi_R\rangle$ by rapid adiabatic following across the avoided-crossing.
- The chiral nature of the bound state can direct quantum information either to the left or the right qubit via dipole-dipole interaction.

## Waveguide fabrication

a)

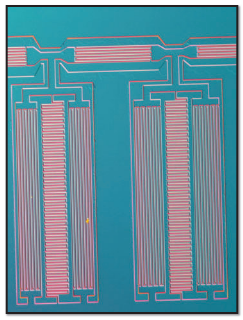

b)

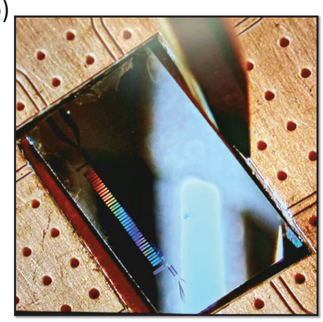

- Each site of the waveguide is formed by a lumped-element resonator in co-planar design.
- The fabrication is done by standard bi-layer liftoff processes followed by Aluminum evaporation.
- Figure (b) is microscope image of a unit-cell. Figure a) is the chip containing 19 coupled resonators that forms waveguide

## Transmission measurement

a)

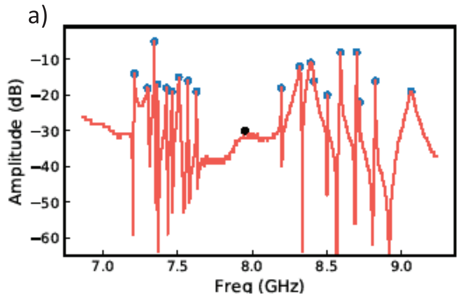


b)

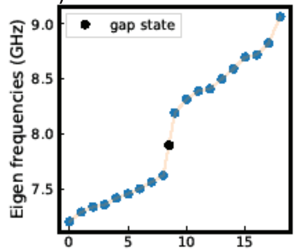


- Transmission measured through the waveguide shows peaks corresponding to all the 19 resonators and a bandgap from 7.75 GHz to 8.45 GHz. The bound state appears in the bandgap which can be tuned by coupling to a qubit.
- In Fig b) the frequencies of each peak is plotted to show the spectrum of the fabricated qubit with a bandgap and a bound state in the center of the gap.

## Conclusion

- Looking forward we envision to demonstrate 3-qubit directional quantum state transfer experimentally.
- The chiral quantum system that we designed can also be used for studying novel many-body quantum phenomenon like chiral quantum spin liquids.

**Title:** Chiral quantum state transfer in waveguide QED

**Candidate:** Pradeep Nandakumar

**Abstract:**

Coherent transfer of information between qubits is fundamental to achieving any quantum information processing task. Here we discuss experimental progress towards developing a tunable chiral quantum system that allows us to select the direction in which the quantum information is shared between qubits. The directional qubit-qubit interaction is achieved via photonic bound states that live in a waveguide composed of an array of coupled cavities. The bound state is induced in the bandgap by suitably engineering the tunnel couplings and on-site potentials of the cavities in the array. In-situ control of the chirality of the bound states is achieved by a frequency tunable Transmon qubit coupled to the central site of the waveguide.

# Dark matter detection via atomic interactions

A. R. Caddell, B. M. Roberts

School of Mathematics and and Physics,
The University of Queensland, Brisbane, Australia

## What is Dark Matter?

- Around 30% of the Universe is matter, but we can only see 5% of it. Dark matter (DM) is the proposed 25% that remains [1]
- Evidence for DM is extensive: rotation curves, gravitational lensing, large scale structure simulations, CMB, BBN, and galaxy surveys all point to a missing mass [1]
- DM must interact primarily via gravity, but may have some small coupling to ordinary matter
- Undetected, as of yet
- Most popular particle DM candidate are Weakly Interacting Massive Particles (WIMPs)

## Direct Detection

- Scintillation is main detection route for DM
- Dual-phase time projection chambers contain liquid and gaseous forms of scintillating material
- S1 signals are the first scattering events in liquid region
- Ionised electrons from first event drift up to gas region, where second event occurs and gives off S2 signal
- Current experiments need S1 and S2 signals combined to get the recoil energy [2]

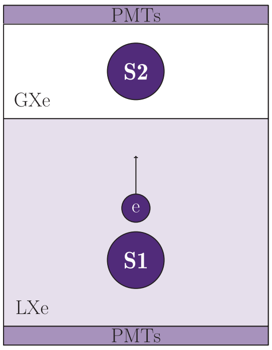


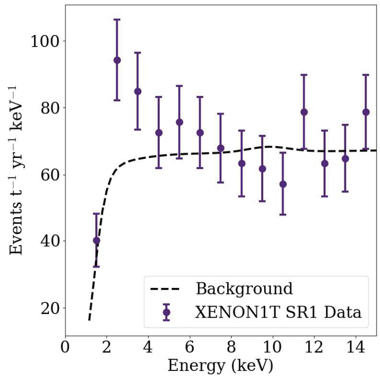


## Electron-Interacting sub-GeV Dark Matter

- Nuclear recoils from sub-GeV DM-nucleon scattering event too weak for detection with current experiments
- A scattering event between a DM particle and a bound electron could lead to ionisation
- S1 signal of DM-electron scattering near the low-energy threshold of current detectors, so would mostly appear as S2-only signal [4]
- Possibility for S1 signal detections with future detectors [4]

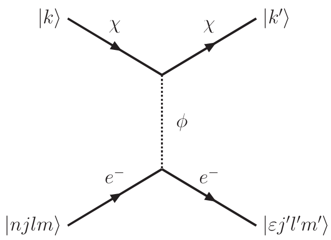


To find cross-sections and event rates, we need to find the atomic excitation factor,

$$K_{njl} = E_H \sum_m \sum_f \left| \langle f | e^{i\vec{q}\cdot\vec{r}} | njlm \rangle \right|^2 \mathcal{Q}_f(E)$$

When calculating $K_{njl}$,

1. Initial states, $|njlm\rangle$, need relativistic wavefunctions [3] [5]
   - The initial state electrons are bound, and are very fast close to the nucleus
2. Final states, $|f\rangle$, cannot be approximated as plane waves
   - Sommerfeld enhancement needs to be considered
   - Attractive potential makes wavefunctions differ from plane waves near nucleus, an important region for DM-electron scattering [4]

## Preliminary Results

So far...

- $K_{njl}$ is a 2D function, but can be approximated as step function (zero when energy deposition is less than ionisation energy, $I_{njl}$),
$$K_{njl}(q, E) = K_{njl}(q)\Theta(E - I_{njl})$$
- When the energy deposition goes above the ionisation energy of an orbital, that orbital is able to be ionised in a collision with a DM particle
- This approximation is promising for some important regions of the parameter space
- Less accurate for outer electrons (low ionisation energies) at high energy deposition, but these contribute little to total $K$
- Cross-sections currently underestimated, but can be compensated for by tuning $E$
- Computationally faster when using pre-calculated tables for $K_{njl}(q)$

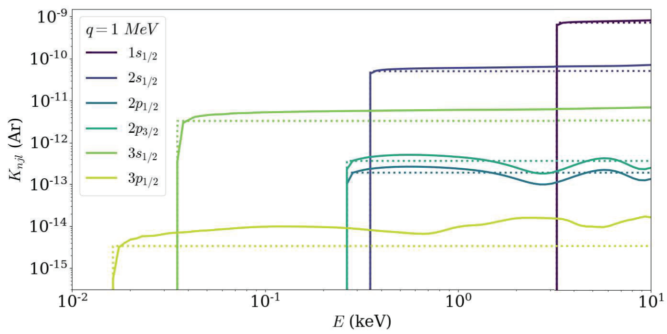


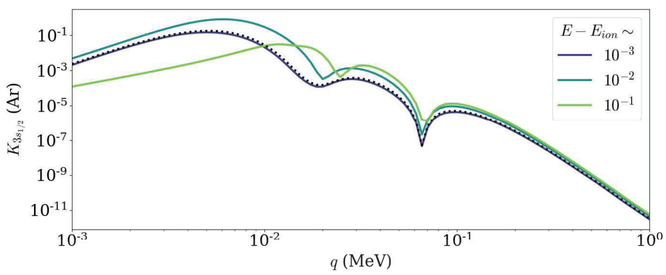


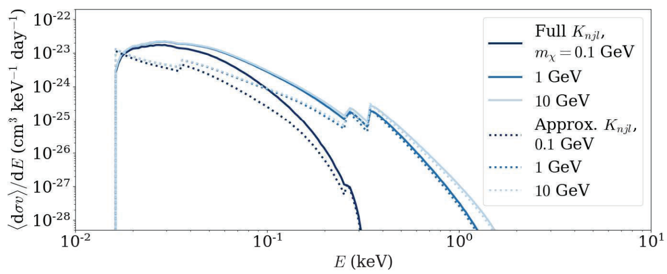


## Future Work

- Calculate event rates for argon and xenon
- Release table of atomic excitation factors across range of $q$-values for public use
- Prepare code for public release
- Include many-body effects in calculations

## References

[1] N. Aghanim and et al. *Astronomy & Astrophysics*, 641:A6, 9 2020.
[2] E. Aprile and et al. *Physical Review D*, 102(7):72004, 2020.
[3] B. M. Roberts, V. A. Dzuba, V. V. Flambaum, M. Pospelov, and Y. V. Stadnik. *Physical Review D*, 93(11):1–22, 2016.
[4] B. M. Roberts and V. V. Flambaum. *Physical Review D*, 100(6):63017, 2019.
[5] B. M. Roberts, V. V. Flambaum, and G. F. Gribakin. *Physical Review Letters*, 116(2):1–5, 2016.

**Title: Dark matter detection via atomic interactions**
**Candidate:** Ashlee Caddell

**Abstract:**
We investigate low mass WIMPs (at the GeV scale) and their potential for direct detection via atomic interactions. Due to these WIMPs having masses comparable to nucleons, detection of any nuclear recoil in scintillation experiments proves difficult. Instead, a WIMP-electron interaction resulting in atomic ionisation could be detected in conventional scintillators due to an enhanced scattering rate. Considering this possibility is important for assessing recent experimental results and upcoming scintillator-based dark matter searches.

# Investigating Gravitational Wave Cosmology with Simulated Data

Liana Rauf ,Cullan Howlett Tamara Davis
School of Mathematics and Physics, University of Queensland, Brisbane, QLD 4072, Australia

Gravitational waves are a new window to the universe, but there are mysteries surrounding the sources that host them. This is where simulations come in! We show how simulating black hole formation and evolution over the lifetime of the universe can be used to predict the populations of gravitational waves, that are out there in galaxies, waiting to be discovered. Using simulations also enables us to test of a wide range of stellar evolution models, to analyse their effect on the merger rate.

## What are Gravitational Waves?

Gravitational waves are ripples in spacetime, carrying energy and momentum. They can be described as circularly polarised waves, which distort objects that they interact with. In 2015, the LIGO and Virgo interferometers first detected gravitational waves from the merger of two black holes (GW150914). The signal shows the strain data, which is the relative change in length of the interferometer arms (see Figure 1).

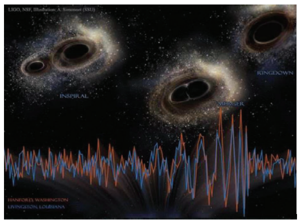


**Figure 1:** The three distinct phases of the binary black hole merger are the inspiral, merger and ringdown. The sharp spike in the signal at the point of the merger is known as a "chirp" [1].

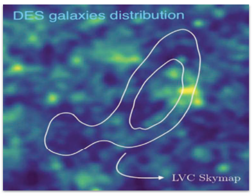


**Figure 2:** Galaxy distribution in DES coloured by the stellar mass. The contours show the probability of the observed region containing the GW event source GW170814 [2].

The signal contains information about the properties of the binary system, which can answer fundamental questions about black hole formation and stellar evolution such as:

- What is the black holes mass and spin distribution throughout the Universe?
- What is the merger rate as a function of redshift?
- What are the formation channels for compact binaries?

The scope of gravitational waves is large and will revolutionise our understanding of the Universe. Future gravitational wave detectors will survey the complete range of compact binaries, so cosmological simulations will be essential in understanding these observations. These results will be useful for future surveys in their follow-up of gravitational wave sources by only targeting galaxies that are likely to host gravitational wave events, as shown in Figure 2.

## Approach: From Birth to Collision

### COMPAS

COMPAS (*Compact Object Mergers, Population, Astrophysics and Statistics*) [5] is a population synthesis tool for generating and tracking binaries throughout their lifetime, and exploring uncertainties in stellar evolution models.

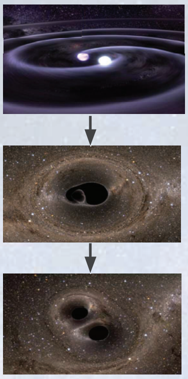

### SHARK

SHARK [3] is a semi-analytic model describing key processes in galaxy formation and evolution within a cosmological volume.

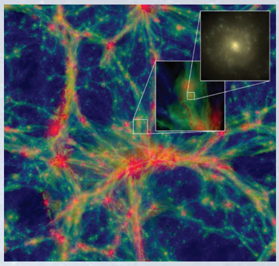

**Figure 3:** Simulation of the dark matter haloes in which galaxies are built [4].

We combine COMPAS and SHARK to produce the merger rate (number of gravitational wave events per year) as a function of time. We can then apply this method to *all* galaxies in the SHARK simulation.

**Older galaxies with high stellar mass and star formation rate are more likely to host GW events.**

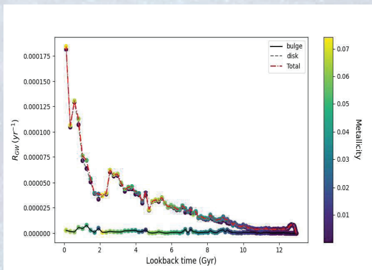


## Comparing to Observations

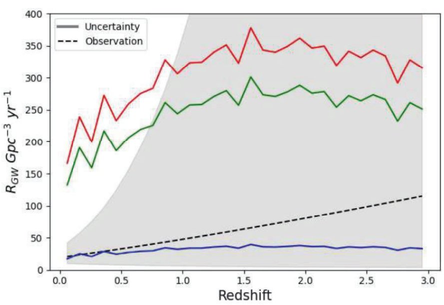


Black hole mass model 1 [6]

Orbital separation model [7]

Black hole mass model 2 [8]

**Figure 7:** The plot shows the merger rate density (number of gravitational wave events per year, per unit volume) as a function of redshift. The uncertainty in stellar evolution models can *significantly* affect the gravitational wave rate!

**References:** [1] LIGO, NSF, A. Simonnet (SSU) [2] Soures-Santos et. al 2019 (arxiv: 1901.01540) [3] Lagos et. al 2018 (arxiv: 1807.11180) [4] Schaye et. al 2014 (arxiv: 1407.7040) [5] Stevenson et. al 2017 (arxiv: 1704.01352) [6] Fryer et. al 2011 (arxiv: 1110.1726) [7] Sana et.al 2012 (arxiv: 1203.2156) [8] Hurley et. al 2000 (arxiv: astro-ph/0001295)

**Title: Investigating Gravitational Wave Cosmology with Simulated Data**

**Candidate:** Liana Rauf

**Abstract**:

Gravitational waves are a new window to the universe, but there are mysteries surrounding the sources that host them. This is where simulations come in! We show how simulating black hole formation and evolution over the lifetime of the universe can be used to predict the populations of gravitational waves, that are out there in galaxies, waiting to be discovered. Using simulations also enables us to test of a wide range of stellar evolution models, to analyse their effect on the merger rate.

# Can You Paddle in a Superfluid?


Maarten T.M. Christenhusz[1,2,†], Matthew Reeves[1,2], Arghavan Safavi-Naini[3], Halina Rubinsztein-Dunlop[1,2], Matthew J. Davis[1,2], Tyler W. Neely[1,2]

[1]ARC Centre of Excellence for Engineered Quantum Systems, University of Queensland, Brisbane, 4072, Australia

[2]School of Mathematics and Physics, University of Queensland, Brisbane, 4072, Australia

[3]Institute for Theoretical Physics, University of Amsterdam, Science Park 904, 1098 XH Amsterdam, the Netherlands

website: **http://bec.equs.org** †email: m.christenhusz@uq.edu.au


## Introduction

Superfluids are known for their characteristic absence of viscosity. The absence of viscosity in term results in a flow without loss of kinetic energy. The extraordinary behaviour of superfluids makes the study of their dynamical behaviour an interesting area of research, especially when comparing their behaviour to macroscopic fluid phenomena. In this work we investigate turbulence and drag forces inside a wake in a superfluid. Does a superfluid flow pas a barrier the same way a normal fluid does? In the absence of viscosity, can we define a Reynolds number [1]? Furthermore, considering no kinetic energy is lost in the flow, is there drag in a superfluid? Is it even possible to paddle in a superfluid?


## Numerical Implementation

We assume our superfluid BEC to be at zero temperature. To introduce a flow, we solve the open-dissipative Gross-Pitaevskii equation (ODGPE):

$$i\hbar\delta_t\psi(\mathbf{r},t) = \mathcal{L}\psi(\mathbf{r},t) - i\gamma(\mathbf{r})\left[\mathcal{L} - \mu(\mathbf{r})\right]\psi(\mathbf{r},t)$$

with $\mathcal{L}$ the Gross-Pitaevskii operator:

$$\mathcal{L} = -\frac{\hbar^2}{2m}\nabla^2 + V(\mathbf{r},t) + g\left|\psi(\mathbf{r},t)\right|^2.$$

The ODGPE is a damped GPE with a source and drain for the BEC. The source and drain have a spatially dependent chemical potential, $\mu(\mathrm{r})$, that induces a flow through the system [3].

The spatially dependent $\mu(\mathrm{r})$ can be a smooth function, or in the case of our work, consist of two step functions as depicted below. For the case when $\mu_1 > \mu_2$, the superfluid flows from left to right with a velocity $u$.

The advantage of using the ODGPE over a commonly used GPE in a moving frame is the ability to induce flows in more complex geometries, such as ring traps, and the simple experimental implementation.

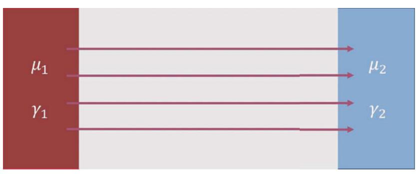


## Drag forces and Vortex Shedding

In our study, we analyse the formation of Von Kármán vortex streets for various kinds of barrier shapes, $V(\mathbf{r})$. Classically, a large drag is associated with flat plates and triangle or prism-like shapes. The drag force on a body is given by:

$$F_\mathrm{d} = \frac{1}{2}\rho u^2 c_d A,$$

with $u$ the velocity and $c_d$ the drag coefficient. Barriers with a large drag coefficient, such as a flat plate, show vortex shedding at low velocities, $u$.

The relation between shedding frequency and wake velocity is described by the Strouhal number, and is given by

$$\mathrm{St} = \frac{fD}{u},$$

with $f$ the frequency of vortex shedding and $D$ the barrier size. We compare the relation between the Strouhal and Reynolds number for a superfluid and compare it with a classical fluid.

The shedding of vortices implies momentum transfer between the superfluid and barrier and as such, the existence of a drag force. The existence of a superfluid drag force would then confirm we can paddle in a superfluid!

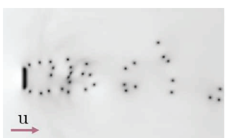



## Quantum vs the macroscopic world

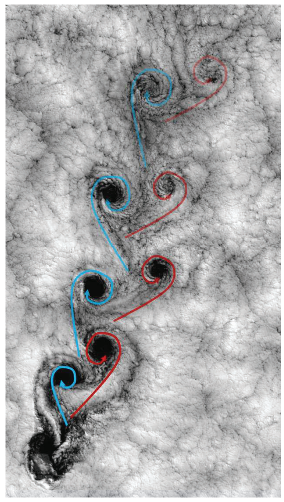

Macroscopically, two types of Von Kármán vortex streets are observed: charge-2 (K2) vortex streets – which are characterized by formation of clockwise-counter clockwise vortices – and irregular vortex streets. The latter are characterized by the chaotic and turbulent motion of clusters of vortices. The K2-regime can be observed in clouds off the Chilean coast neat the Juan Fernandez Islands [4].

On a quantum scale, the same K2 and irregular regimes are observed. Additionally, a regime is observed in which vortices are released obliquely from the obstacle (OD). The dynamical similarities between classical and quantum fluids seem to imply that, while there is no viscosity and dissipation in a quantum fluid, we still observe turbulence in a quantum fluid.

## Comparing Quantum and Classical

A study by Roshko [5] in 1954 compares the drag and shedding frequency of various two-dimensional bodies, such as circular cylinders, wedges and rectangular plates.

The data obtained using a wind-tunnel follows similar behaviour to our numerically obtained data. Simulations on different barrier shapes and future experiments will further verify the dynamical similarities between quantum and classic systems.

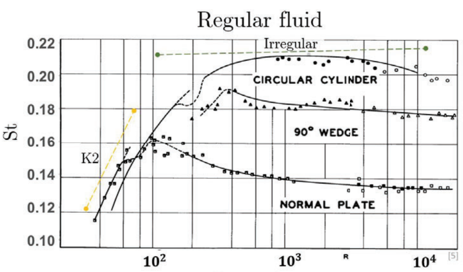


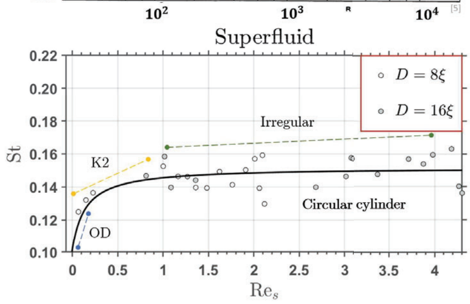


## References


[1] Reeves, M. et al, Identifying a Superfluid Reynolds Number via Dynamical Similarity, *Phys. Rev. A* 10.1103 (2015).

[2] Wagner, J. (2014).

[3] Deng, Z. et al, Non-equilibrium States of one-dimensional Bose-Einstein Condensate at Zero Temperature Coupled to Density Reservoirs, *Unpublished*.

[4] Cahalan, B. NASA GSFC, (1999).

[5] Roshko, A, On the Drag and Shedding Frequency of Two-Dimensional Bluff Bodies *NACA Report No. 3169, National Advisory Committee on Aeronautics* (1954).

**Title:** Can You Paddle in a Superfluis?

**Candidate:** Maarten Christenhusz

**Abstract:**
Superfluids are known for their characteristic absence of viscosity. The absence of viscosity in term results in a flow without loss of kinetic energy. The extraordinary behaviour of superfluids makes the study of their dynamical behaviour an interesting area of research, especially when comparing their behaviour to macroscopic fluid phenomena. Despite lacking viscosity – and therefore a well-defined Reynolds number -- turbulence is still observed inside superfluids. Moreover, the shedding of vortices inside a superfluid imply a transfer of momentum and as such, the existence of a drag force. While a superfluid flows without loss of kinetic energy, is it possible to paddle in a superfluid?

# A hybrid quantum chemical machine

A. Muniraj Saraswathy[1], L. A. Williamson[1], A. Safavi-Naini[2], M. J. Davis[1]
1. ARC Centre of Excellence for Engineered Quantum Systems, School of Mathematics and Physics, The University of Queensland, QLD 4072, Australia.
2. Institute of Theoretical Physics, The University of Amsterdam, Science Park 904, 1098 XH Amsterdam, the Netherlands.

## 1. Goals

We are interested in addressing the following questions:

- How would a quantum machine operating between two heat/chemical reservoirs work?
- What changes occur when chemical work is included in addition to mechanical work when designing protocols?

Our work is motivated by experiments with ultracold gases as a model system similar to the idea by Gluza et.al.[1]

## 2. Chemical Work

Work done in transferring dN particles from a high chemical potential reservoir to one with a lower chemical potential.[2]

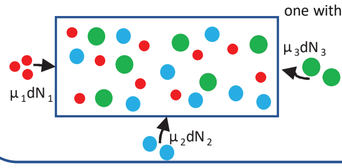


Total chemical work is

$$\sum_i \mu_i dN_i$$

## 3. Key Points

- A weakly interacting Bose gas system operating between two chemical reservoirs at zero temperature converts all mechanical work to chemical work.[3]
- Operating machines at finite temperatures is not straight forward: it includes hybrid machine operation and spontaneous heat and particle exchange steps.
- To gain an initial understanding, we analytically study engine protocols using a trapped ideal gas system.

## 4. Constant temperature cycle

### A. Zero temperature engine (weakly interacting Bose gas)[3]

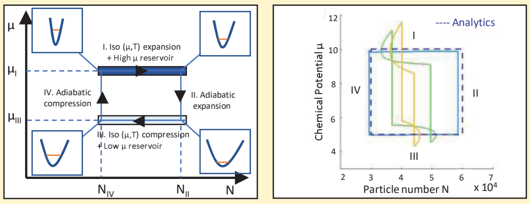


$\mu$ vs $N$ plot

$W^{mech} = -W^{chem}$

Chemical engine (Bose gas in a 3D harmonic trap) is operated between two reservoirs at zero temperature, one at a higher and another at a lower chemical potential.

### B. Finite temperature engine (ideal gas)

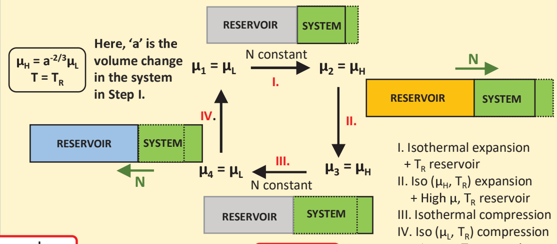


$dQ = 0$

The engine is operated between two reservoirs at finite (but constant) temperature, one at a higher and another at a lower chemical potential. For simplicity, the model system is an ideal gas system trapped in a three dimensional box.

## 5. Incorporating both heat and particle flows: hybrid machines

### A. Constant chemical potential to temperature ratio

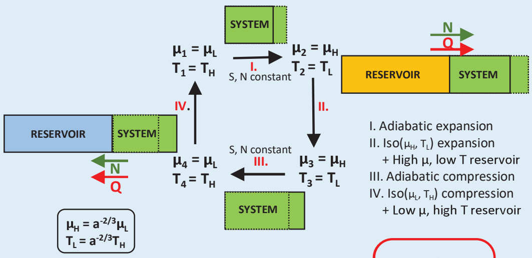


Total $(W^{mech} + W^{chem} + Q) = 0$

$W^{mech} > 0$
$W^{chem} > 0$
$Q < 0$

- The system is operated between two reservoirs at different chemical potentials and temperatures. The protocol preserves the system's μ/T ratio throughout the cycle.
- *The system properties match the reservoir properties at the time of contact.*
- The system uses heat to perform mechanical and chemical work - a hybrid engine/ particle pump.

### B. Variable chemical potential to temperature ratio

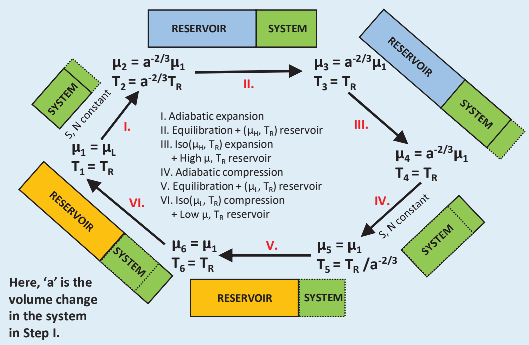


When $T_2 < T_1$ and $\mu_2 > \mu_1$

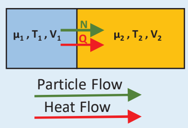


- Both the reservoirs are at the same temperature $T_R$ but at different chemical potentials.
- *The system and reservoir properties cannot be matched at the time of contact.*
- On contact, the system spontaneously exchanges heat and particles until equilibrium is attained.
- Depending on the amount of volume change, μ/T ratio and the $\mu_H/\mu_C$ ratio, the system can function as an engine/pump or both.

**Open questions:**

- How to explain the fact that the system has different functions depending on the parameters?
- How can we model the nonequilibrium behaviour of the spontaneous step?

## 6. Future work

- Extending the finite temperature analysis to an interacting Bose gas using SPGPE simulations.
- Identifying parameters in the protocol that maximize machine performance.
- Including quantum effects like correlations and coherences into the system to study its effects on machine performance.

Contact: a.munirajsaraswathy@uqconnect.edu.au

**References:** [1]. *Quantum field thermal machines*, Gluza et.al., PRX Quantum **2**, 030310 (2021).
[2]. *Efficiency at maximum power of a chemical engine*, Hooyberghs et.al., J. Chem. Phys. **139**, 134111 (2013).
[3]. *Non-equilibrium thermodynamic transformations of Bose gases*, Joshua Guanzon, Title, B.Sc. (Hons) thesis, University of Queensland (2018).

**Title:** A hybrid quantum chemical machine.

**Candidate:** Abitha Muniraj Sarawathy

**Abstract:**

Quantum heat machines are devices consisting of a single or many-body quantum system as their working medium and convert different forms of energy to useful work. We present a cyclic protocol for such a hybrid machine with a Bose/ideal gas in a three-dimensional trap as its working fluid. This machine undergoes a four-stroke process between two reservoirs that are at different temperatures and chemical potentials. In each cycle, there is an exchange of heat, chemical work, and mechanical work between the system and the reservoirs. Depending on the nature of the process it undergoes (such as adiabatic, isothermal, or isochemical), the system can function either as an engine, refrigerator, heat pump, a particle pump or can have multiple functions simultaneously. We analytically characterize the performance of the Bose/ideal gas thermal machine for several cycles and summarise the principles of machine design. We also perform numerical simulations of the machines using classical field methods namely, the Stochastic Projected Gross-Pitaevskii equation (SPGPE) technique. Future work will incorporate adding quantum effects (like coherence, entanglement, etc) in the finite-temperature many-body hybrid machine.

# Aberration Corrected Nanofabrication

D.J Armstrong*, A.B Stilgoe, T.A Nieminen, I.Favre-Bulle and H.Rubinsztein-Dunlop

Optical Micromanipulation Group, School of Mathematics and Physics
The University of Queensland, St. Lucia, QLD, 4067

## Abstract

Using a femtosecond laser and a spatial light modulator (SLM), we are able to produce high-resolution micron-scale structures for optical trapping experiments through two photon photopolymerization (2PP). Incorporating an SLM allows for a versatile, tunable system that takes into account all aberrations throughout the optical train, enabling precise, dynamic power control for nanofabrication using multiple sub-diffraction-limited spots. These structures have a wide range of applications in optical trapping experiments and are used in the study of micron-scale biological systems.

## Introduction

2PP is the process of polymerizing resin using a focused, high intensity pulse laser. A photo-initiator molecule (I) transforms into a pair of free radicals via photon absorption:

$$I + h\nu \rightarrow I^* \rightarrow 2R^*$$

These free radicals combine with a monomer molecule (M) to produce a chain-initiating molecule (M*), which then reacts with other monomers:

$$R^* + M \rightarrow M^*$$

A focused laser produces a sub diffraction-limited volume exceeding the polymerization threshold, producing ellipsoid-shaped voxels which can be stacked to produce microscopic structures.

## 2PP Voxels

Voxel resolution is determined by factors such as exposure time, laser intensity and the numerical aperture of the microscope objective used. Typical voxels are ~150nm in diameter and ~500nm in length.

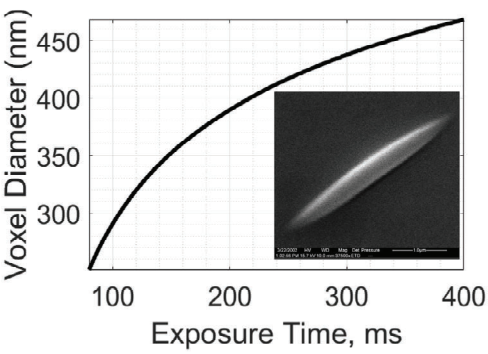


Figure 1: (top) Voxel size as a function of exposure time, (inset) sample voxel [1] printed on top of a microscope slide. (bottom) Intensity above, at, and below polymerization threshold.

## Structure examples

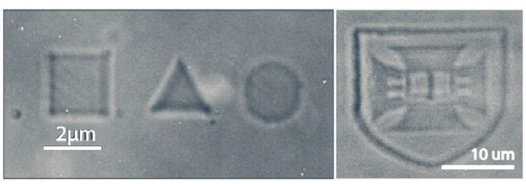


Figure 2 (left) Simple shapes formed with 2PP. (right) UQ logo ~20um wide and 1um talll.

## Experimental Setup

The Ti Saphire laser producing pulses ~80 fs long at a repetition rate of 80 MHz. A 512 x 512 SLM is utilised with high numerical aperature (1.4 NA) objective and a nanopositioning stage. The printing process is monitored in real-time using a CCD camera illuminated with a blue LED.

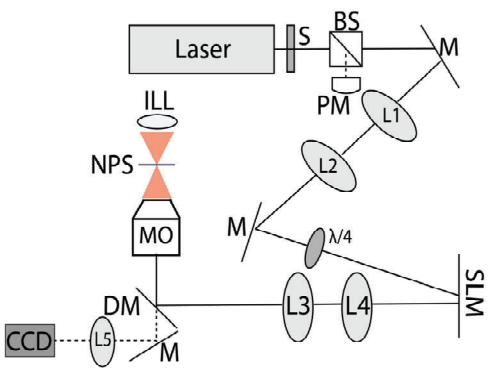


Figure 3: Diagram showing experimental setup. Abbreviations: S - shutter, BS - beam splitter (90/10), PM - power monitor, M - mirror, L - lens, λ/4 - quarter waveplate, SLM - spatial light modulator, DM - dichroic mirror, MO - microscope objective, NPS - nanopositioning stage, CCD - charged coupled device, LL- illumination.

## Aberration Correction

Imperfections throughout the optical train cause aberrations in the focused spot, significantly affecting print quality by dispersing the focused volume [2]. By measuring distortions in the imaging plane, a system-specific phase correction can be applied to account for any distortions which may arise throughout the entire optical train [3].

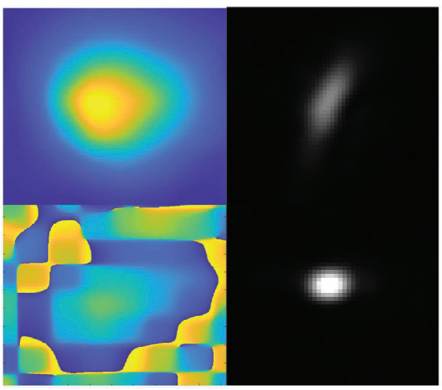

Figure 4: (top) (left) Laser beam amplitude measured at SLM. (right) Uncorrected elliptical spot formed without aberration correction. (bottom) (left) SLM phase pattern used to correct distortions. (right) Aberration corrected spot.

## Printing with an SLM

Using an SLM allows for dynamic power control, which helps reduce deformations for multi-layered structures, as well as a significant decrease in printing time due to being able to utilise multiple spots for simultaneous polymerization volumes.

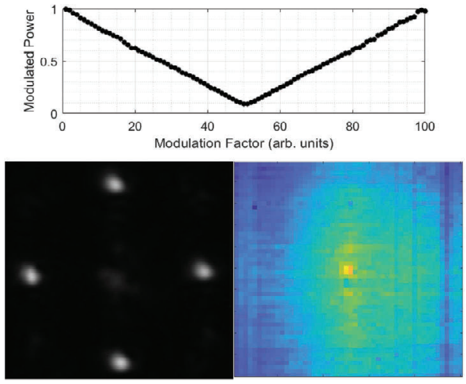


Figure 4: (top) Power control through amplitude dithering using an SLM. (bottom) (left) Four spots from single laser beam used to speed-up printing process. (right) Lookup table showing position-dependent power from diffracted laser spot.

## Structures for OT Experiments

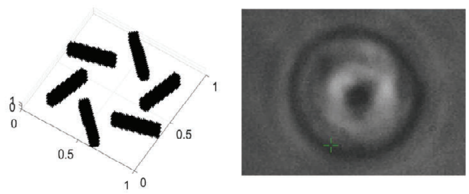


Figure 6: (left) Sample bitmap fed plane-by-plane into SLM, designed to filter motile bacteria by helicity. (right) Shape induced birefringent sphere for measuring viscosity.

We are currently producing birefringent structures to be used for high speed viscosity measurements, along with barriers to test theories of bacterial propulsion.

## Referenecs

[1] Theodor Asavei.Optically Fabricated and Driven Micromachines. PhD thesis, 2010.

[2] Lor and Kelemen, Pal Ormos, and Gaszton Vizsnyiczai. Two-photon polymerization with opti-mized spatial light modulator. Journal of the European Optical Society, 6,2011.

[3] Alexander Stilgoe and Halina Rubinsztein-Dunlop. Wave characterisation and aberration cor-rection using hybrid direct search.Journal of Optics, 2021.

**Title:** Aberration Corrected Nanofabrication

**Candidate:** Declan Armstrong

**Abstract:**

Using a femtosecond laser and a spatial light modulator (SLM), we are able to produce high-resolution micron-scale structures for optical trapping experiments through two-photon-photopolymerization (2PP).

Incorporating an SLM allows for a versatile, tuneable system that takes into account all aberrations throughout the optical train, enabling precise, dynamic power control for nanofabrication using multiple sub-diffraction-limited spots. Structures produced using this technique have a wide range of applications in optical trapping experiments and are used in the study of micron-scale biological systems.

# Many-Body Dynamics of Ultracold Polar Molecules in an Optical Lattice

**T. J. Harris**[1], A. Safavi-Naini[1,2], A. J. Groszek[1] and M. J. Davis[1]

1. ARC Centre of Excellence for Engineered Quantum Systems, School of Mathematics and Physics, The University of Queensland, Brisbane, QLD 4072, Australia.
2. Institute of Theoretical Physics, The University of Amsterdam, Science Park 904, 1098 XH Amsterdam, the Netherlands.

EQUS Australian Research Council Centre of Excellence for Engineered Quantum Systems

THE UNIVERSITY OF QUEENSLAND AUSTRALIA

## Motivation: Quantum magnetism in ultracold polar molecules

- Ultracold polar molecules pinned in an optical lattice realize long-range anisotropic dipolar interactions $V(r) \sim 1/r^{\alpha}$, providing a flexible platform to study models of *quantum magnetism*. These systems also present a unique opportunity to study non-equilibrium quantum dynamics in the presence of disorder.
- The dipolar XXZ Hamiltonian ($\hbar = 1$) [1]:

$$\hat{H} = \frac{1}{2}\sum_{i\neq j} V_{ij}\left[\underbrace{J_z \hat{S}_i^z \hat{S}_j^z}_{\text{Ising}} + \underbrace{\frac{J_\perp}{2}\left(\hat{S}_i^+ \hat{S}_j^- + \hat{S}_i^- \hat{S}_j^+\right)}_{\text{Spin-exchange}} + \underbrace{W\left(\hat{n}_i \hat{S}_j^z + \hat{S}_i^z \hat{n}_j\right)}_{\text{Spin-density}}\right]$$

**Anisotropic couplings:** $V_{ij} = \left(1 - 3\cos^2\theta_{ij}\right)/|\mathbf{r}_i - \mathbf{r}_j|^3$

**Spin-1/2 operators:** $[\hat{S}_i^z, \hat{S}_j^{\pm}] = \pm\delta_{ij}\hat{S}_j^{\pm}$

$J_z$: Ising coupling
$J_\perp$: Spin-exchange coupling
$W$: Spin-density coupling

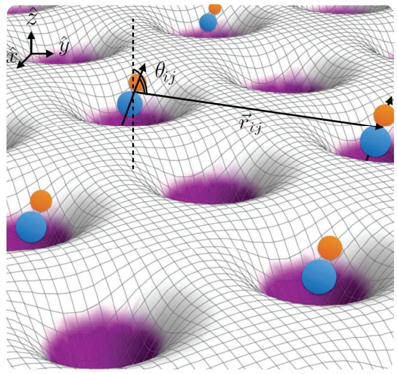


- Disorder in systems of ultracold molecules can manifest in one of two ways [2]:
  (i) A disordered spatial potential can be added to the lattice, e.g using an optical speckle potential; or,
  (ii) if the lattice filling fraction is less than unity, there is natural positional disorder in the arrangement of molecules in the lattice – and consequently in the dipolar couplings.

## Method: Engineering tunable spin-spin interactions

**Rotational level structure:**
- Model molecules as a rigid rotor coupled to a DC electric field.
- Encode spin-1/2 d.o.f in the molecules' rotational states.

**Rigid rotor:** $\hat{H}_0 = B\hat{\mathbf{N}}^2 - \hat{d}_0 E$

**KRb parameters:**
$d = 0.566$ D
$B = 1.114$ GHz

- Dipole moments tunable by E-field
- Access to different spin couplings, including sign & magnitude.

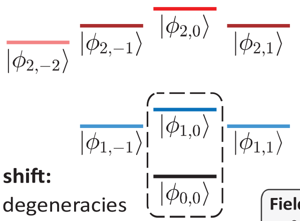


**DC-Stark shift:**
- Breaks degeneracies $|N, M\rangle \rightarrow |\phi_{N,M}\rangle$

**Field strength:** $\beta_{DC} = dE/B$

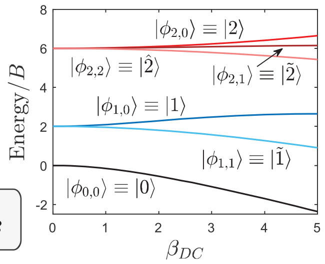


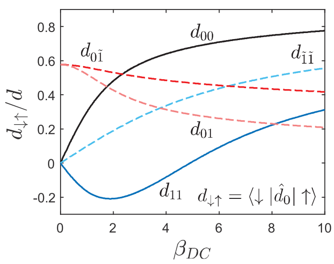


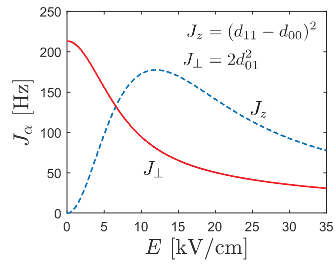


## Results

**Benchmarking the dTWA:**
Dynamics of a 1D spin chain with $N = 100$ spins in the Ising limit ($J_\perp = 0$).
- Comparison of Gaussian TWA, dTWA with analytic solution.

(a) Collapse & revival dynamics
(b) Deviation from exact soln
(c) dTWA shows agreement for select 2-body observables

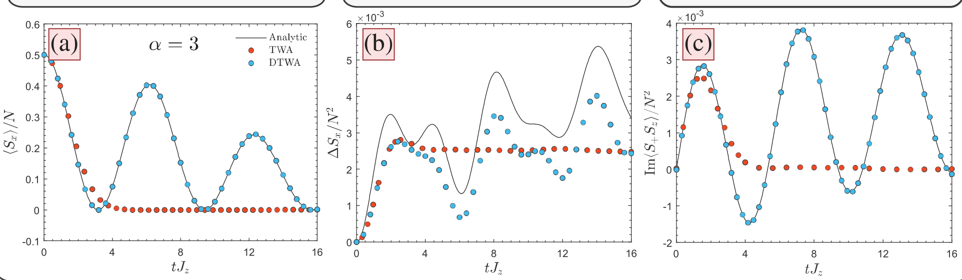


**On-site disorder:**
MBL in the 1D XXX model ($J_z = J_\perp$) for spins subject to random on-site disorder [4].

$I(t) = \sum_i (-1)^i \langle \hat{S}_i^z(t)\rangle$

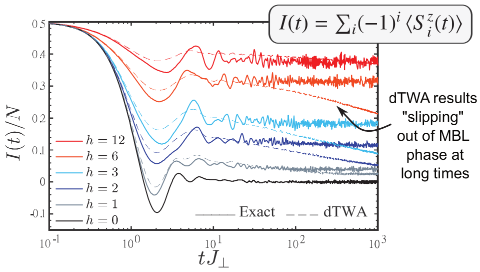


**Positional disorder:**
dTWA simulations of the spin imbalance for dilute gases with different fillings.

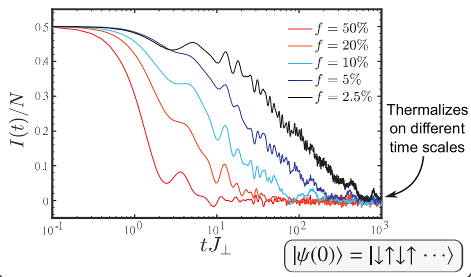


## Conclusions

- dTWA accurately describes dynamics of single and select two-body observables.
- The dTWA **is capable of capturing signatures of MBL** in disordered spin systems:
  - Upper bound for critical disorder strength in the thermodynamic limit given by:

$$h_c \approx 3.5$$

  - Good agreement with ED out to $tJ_\perp \sim 10$.
- Dilute gases of ultracold polar molecules **do NOT** support a localized phase:
  - Thermalization timescale lengthens as filling decreases due to weaker mean coupling.

## Future Work

- Explore interplay of disorder, dimensionality & interactions in systems of polar molecules:
  - 2D and 3D lattice geometries.
  - Long-range interactions i.e. $\alpha < D$.
  - Does MBL persist in these regimes?
- Implement *generalized* dTWA [5], by grouping molecules into clusters:
  - Applicable to current experiments with magnetic atoms e.g. Cr or Dy.
- Introduce spin-density interaction as in [1].

**References:**
[1] Gorshkov et al., Phys. Rev. A **84**, 033619 (2011).
[2] Hazzard et al., Phys. Rev. Lett **113**, 195302 (2014).
[3] Schachenmayer et al., Phys. Rev. X **5**, 011022 (2015).
[4] Safavi-Naini et al., Phys. Rev. A **99**, 033610 (2019).
[5] Zhu et al., New J. Phys. **21**, 082001 (2019).

**Contact: tim.harris@uq.edu.au**

**Title:** Many-Body Dynamics of Ultracold Polar Molecules in an Optical Lattice
**Candidate:** T. J. Harris

**Abstract:**

Following recent advances in the manipulation of atomic, molecular and optical systems, quantum sim-ulators of strongly-correlated many-body lattice models have been realized on a number of experimental platforms, including ultracold gases of neutral atoms [1] and polar molecules [2], as well as arrays of Ry-dberg atoms [3] and trapped ions [4]. In particular, ultracold polar molecules trapped in optical lattices provide a flexible framework to study models of quantum magnetism due to their spatially anisotropic long-range interactions and rich internal structure. The microscopic parameters of these models can be precisely controlled by altering the intensities of the lattice lasers and the application of external fields [5].

One of the challenges with current polar molecule experiments is that it is only possible to achieve lattice

fillings of ;S 50%. Although this is typically considered a limitation of the system, in our work we aim to utilize this feature in order to study non-equilibrium quantum dynamics in the presence of disorder [6]. We model the system as a dipolar XXZ spin-chain, with effective on-site disorder arising from the dilute, randomised configurations of molecules in the lattice. We then simulate the system's evolution using a combination of numerical methods, including exact diagonalisation, matrix product states and the discrete truncated Wigner approximation [7], and characterise the long-time dynamics and eigenstate properties using a variety of observables: the decay of spin imbalance, growth of entanglement entropy and level-spacing statistics. Our preliminary results indicate that the model exhibits a transition from an ergodic to a many-body localized phase for more dilute fillings and increasing interaction strength.

[1] I. Bloch, J. Dalibard and W. Zwerger, *Rev. Mod. Phys.* 80, 885 (2008).

[2] B. Yan et al., *Nature* 501, 521 (2013).

[3] H. Bernien et al., *Nature* 551, 579 (2017).

[4] J. W. Britton et al., *Nature* 484, 489 (2012).

[5] A. V. Gorshkov et al., *Phys. Rev. Lett.* 107, 115301 (2011).

[6] J. L. Bohn, A. M. Rey and J. Ye, *Science* 357, 1002 (2017).

[7] J. Schachenmayer, A. Pikovski and A. M. Rey, *Phys. Rev. X* 5 011022 (2015).

# What Temperature is Schrödinger's Cat?†

Carolyn E. Wood,* Harshit Verma, Dr Fabio Costa & Dr Magdalena Zych

Australian Research Council Centre of Excellence for Engineered Quantum Systems (EQUS), School of Mathematics and Physics, The University of Queensland, Australia

## Introduction: A Superposition of Temperatures

- Temperature & time two important parameters in standard quantum physics
  - → Quantum clocks in superpositions
  - → Insight into quantum and gravity overlap
- What can we learn about temperature from a similar exploration?

## Thermal Channels and Thermalisation

- Probe interacts with bath via unitary evolution
  → Thermalises to temperature of bath

$$\rho_{in} = \rho_S \otimes \rho_B$$

$$\rho_{in} \;—\; \boxed{U} \;—\; \rho_{out}$$

- Effective map on the system (LHS) as Kraus decomposition (RHS):

$$\mathcal{E}(\rho_S) = \sum_{k,l} c_l^B M_{kl} \rho_S M_{kl}^\dagger \qquad M_{kl} = \langle k|U_{SB}|l\rangle$$

## Case 1: Two Baths (Superposition of Channels)

- Quantum-controlled interactions with baths, analogous to Mach-Zehnder interferometer
  - Initial state $\rho = \underbrace{\rho_S}_{\text{Probe}} \otimes \overbrace{(\rho_{B_0} \otimes \rho_{B_1})}^{\text{Baths}} \otimes \underbrace{\rho_C}_{\text{Control}}$
- Final state (after measuring control) is

$$\rho_S^{(\phi)} = \frac{1}{4}\left(\rho_S^{\beta_0} + \rho_S^{\beta_1} + e^{i\phi}\rho_S^{\beta_0}u^0\rho_S u^{1\dagger}\rho_S^{\beta_1} + e^{-i\phi}\rho_S^{\beta_1}u^1\rho_S u^{0\dagger}\rho_S^{\beta_0}\right)$$

$$\rho_S^{\beta_i} = \sum_k c_k^{\beta_i}|k\rangle_S\langle k|_S; \quad \beta_i \equiv \frac{1}{T_i}$$

- Not thermal
- Dependent on
  - states of both baths + initial probe system state
  - local bath unitaries $u^i$
- Visibility

$$\mathcal{V} = \left|\mathrm{Tr}\left\{\rho_S^{\beta_0}\rho_S^{\beta_1}u^1\rho_S u^{0\dagger}\right\}\right|$$

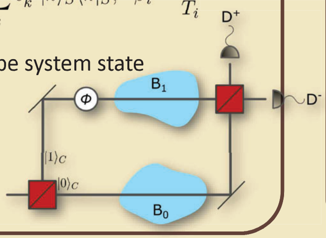


## Case 2: One Bath (Superposition of Purifications)

- Superposition of purifications: $|\Psi\rangle = \sum_i |\psi_{pf}^i\rangle|i\rangle_C$
  - Control state determines temperature of the bath
  - Purifications have the form:

$$|\psi\rangle = \sum_{x=0,1}\frac{1}{\sqrt{2}}\sum_b e^{-i\phi_x}\sqrt{c_b^{B_x}}\,\underbrace{|b\rangle_A}_{\text{Ancilla}}\underbrace{|b\rangle_B}_{\text{Bath}}\underbrace{|x\rangle_C}_{\text{Control}}$$

- Final state

$$\tilde{\rho}_S^{(\phi)} = \frac{1}{4}\left[\rho_S^{\beta_0} + \rho_S^{\beta_1} + 2\sqrt{\rho_S^{\beta_0}\rho_S^{\beta_1}}\left|\mathrm{Tr}_S\left\{u^0\rho_S u^{1\dagger}\right\}\right|\cos(\phi)\right]$$

  - Can be thermal (if $\beta_0 = \beta_1$)
  - Still dependent on local unitaries
- Visibility $\tilde{\mathcal{V}} = \sum_b \sqrt{c_b^{\beta_0}c_b^{\beta_1}}\left|\mathrm{Tr}_S\left\{u^0\rho_S u^{1\dagger}\right\}\right|$

## Partial and Pre-Thermalisation

- Collisional model of gradual thermalisation
  → Successive application of $U_{SB}$
- Each interaction occurs in finite time, with interaction parameter $\eta < 1$

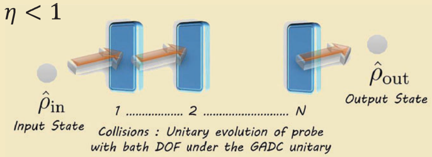


- Changes in $\eta$ alter number of collisions to reach full thermalisation

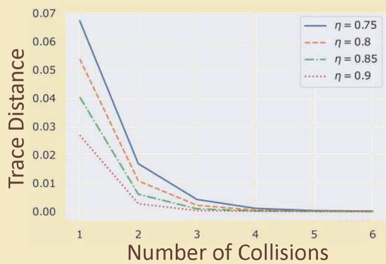


## Results: Comparing Cases through Visibility

- Visibility as an indicator of 'temperature coherence'
- Two-bath case $\quad \mathcal{V} = \left|\mathrm{Tr}\left\{\rho_S^{\beta_0}\rho_S^{\beta_1}u^1\rho_S u^{0\dagger}\right\}\right|$
  - No thermalisation
  - Low visibility, except at low temps
- One-bath case $\quad \tilde{\mathcal{V}} = \sum_b \sqrt{c_b^{\beta_0}c_b^{\beta_1}}\left|\mathrm{Tr}\left\{u^0\rho_S u^{1\dagger}\right\}\right|$
  - Thermalisation possible
  - Max. visibility possible, except when one temperature low

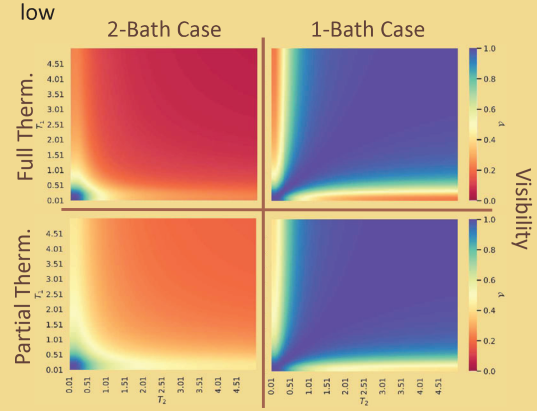


## Summary and Conclusions

- Two cases of a 'Superposition of Temperatures'
  - Two separated baths: thermalisation suppressed
  - One bath in superposition: thermalisation can be reached
  - Both depend on local unitaries
- Implications:
  - Pathway to greater understanding of bath dynamics
  - Sensitivity to local unitaries
- Future directions
  - Unruh-deWitt detectors
  - Tolman-Ehrenfest effect

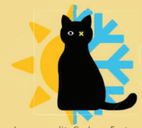

Image credit: Graham Foster

*carolyn.wood@uqconnect.edu.au

**Title:** What Temperature is Schrodinger's Cat?

**Candidate:** C.E. Wood

**Abstract:**

In the context of quantum thermodynamics-where thermodynamical quantities are associated with quantum systems-a question arises whether the notion of temperature can be associated with quantum features, in analogy to whether the notion of time can exhibit quantum features when it is associated with a clock that is itself a quantum system.

In this work we explore two scenarios in which the notion of a 'superposition of temperatures' may arise. In the first scenario, the probe system interacts with different baths depending on the state of another quantum system. In the second scenario the system interacts with only one bath, but the bath along with its purification is now correlated with another quantum system. The bath temperature is dependent on the state of this additional, control, degree of freedom (DoF). In both cases we derive the final state of all systems and discuss conditions for thermalisation of the probe and for temperature coherence-understood as coherence in the DoF on which the temperature depends. We show that the two cases are surprisingly different: For example, in the first scenario the probe does not thermalise and the temperature coherence is reduced even when the bath states are identical, at the same temperature. In the analogous equal-temperature case in the second scenario, the probe can thermalise and reach maximal coherence. We also find that the final probe states depend on the physical context and even physical realisation of the thermalising channels-being sensitive to the particular Kraus representations of the channels-which may explain some of the results obtained in the context of quantum interference of relativistic particle detectors thermalising with Unruh/Hawking radiation. Our results extend to partial and pre-thermalisation, which we study by introducing a collisional model of thermalising interactions between the system and the bath(s).

# Machine Learning Optimised Persistent Currents In BECs

Simeon Simjanovski[1,†], Guillaume Gauthier[1], Matthew Davis[1,2], Halina Rubinsztein-Dunlop[1] and Tyler Neely[1]

[1] ARC Centre of Excellence for Engineered Quantum Systems, University of Queensland, Brisbane, AU.

[2] ARC Centre of Excellence for Future Low-Energy Electronics Technologies, University of Queensland, Brisbane, AU.

website: **http://bec.equs.org** [†]email: s.simjanovski@uqconnect.edu.au

**Introduction:** The rapid development of machine learning technology over recent decades has provided a number of promising advancements for experimental science [1, 2, 3]. Machine learning algorithms have become a powerful tool in scientific research since they suppose no bais or preconceptions about they systems they are modelling which can lead to novel and counter-intuitive solutions [4]. Here, we apply machine learning approaches [6] for the generation of persistent currents in 2D ring trapped BECs through stirring.

## Motivation:

A persistent current in a BEC superfluid constitutes the basis for a kind of matter-wave interferometer, upon which highly sensitive measurements can be made on rotation, inertia or even gravity with sensitivity improved by a factor of ten orders of magnitude over modern photon-based interferometers while maintaining compactness [7, 8]. Persistent currents are often achieved through physically stirring the condensate. Can a set of stirring parameters be found which accurately and efficiently optimise an experimental stirring protocol? **Using machine learning complex optimisations are possible.**

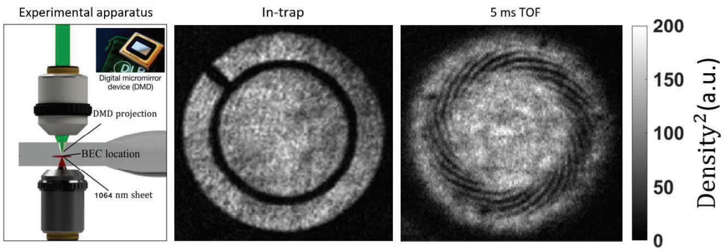


## Experimental implementation:

The available apparatus (left) can trap BECs in almost arbitrary 2D hard-wall configurations using a digital micro-mirror device (DMD) and sheet potential [9]. This allows a persistent current to be generated using a stirring beam (center) subject to the angular profile:

$$\theta(t) = \alpha\left(\frac{t}{400}\right)^2$$

Interference phenomena in free expansion/time-of-flight (TOF) imaging (right) allow for measurement of the system. In the absence of stirring the resulting interference pattern consists of concentric rings. Spiral interference patterns are instead indicative of a winding of the phase of the macroscopic wavefunction (due to stirring here). Fringe number is directly proportional to flow velocity. Vortices in the system are resolvable and appear as black cores in TOF images.

## Machine learning concept:

The machine learner employed was a Gaussian process regression algorithm handled through M-LOOP [6]. Here two cost functions were required for the two types of optimisation considered; target optimisation and maximisation. Both optimisations were completed over 50 total runs including 20 randomly generated parameters to train the learner. The cost functions take into account fringe number and punish the creation of any vortices in the system:

$$cost = |Fringe\,\# - 20| + Vortex\,\#, \qquad \text{for optimising to a target of 20 fringes}$$
$$cost = -Fringe\,\# + Vortex\,\#, \qquad \text{for maximising fringe number}$$

M-LOOP performed optimisation by associating a cost to each parameter set provided which were comprised of three parameters that uniquely characterise the stirring process. These parameters are labelled numerically in M-LOOP as:

1. **Stirring time** of the barrier after insertion
2. **Removal time** of the barrier after the stirring time
3. $\alpha$ or the **acceleration scaling** of the angular profile

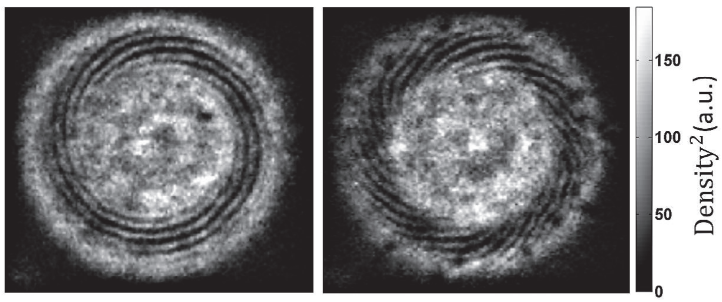


**Cost determination examples.** (Left) High cost due to low fringe number. (Right) High cost due to large vortex number.

## Results from target optimisation.

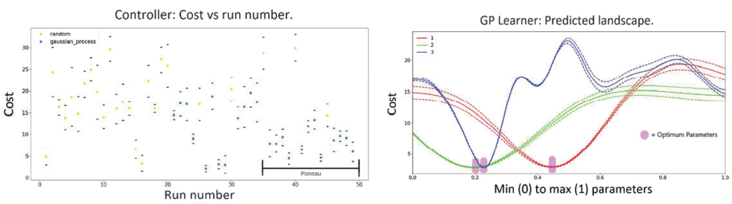


The variation of cost over the different parameters sets/runs shows a sudden decrease of the cost after the initial 20 training runs which quickly plateaus indicating optimisation. The predicted landscape which connects the individual variation of parameters to the associated costs. Minima of the curves represent optimal parameter choices.

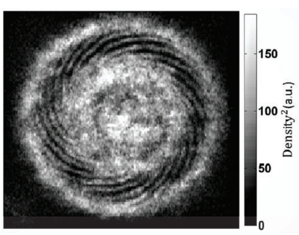


Using optimum parameters, 20 fringes are found in most 5 ms TOF images with a shot-to-shot variation of around $\pm 1$ for both fringes and vortices.

## Results from maximisation.

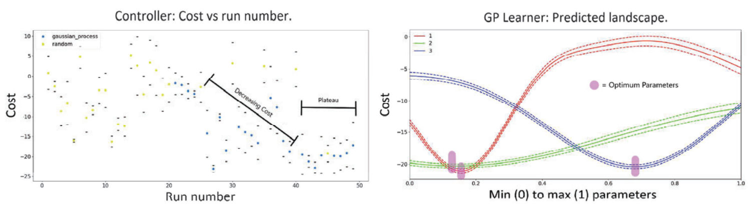


The variation of cost over the different runs shows a steady decrease up to the 40th run after which a plateau effect is observed. This is highly suggestive of steady convergence to the optimum parameter set. The predicted landscape shows the optimum parameters at the minima of the landscape curves.

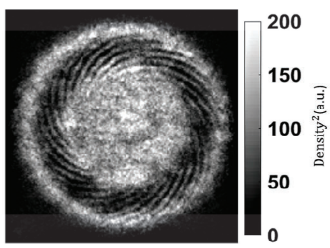


The 5ms TOF images, subject to the optimum parameters, result in around 27 fringes are found here with close to no vortices on average and a shot-to-shot variation of $\pm 1$ for both fringes and vortices.

## Summary.

Both the target optimisation and maximisation were successful in generating the desired persistent currents. The target optimisation clearly achieved the goal of reaching 20 fringes on average, and maximisation suggests to have found that 27 fringes is the upper limit to the flow velocity without invoking excitations. Collectively, the results indicate that machine learning is an accurate and efficient method for controlling persistent currents in 2D BEC superfluids.

## Future Directions.

- Repeat optimisations but introduce a penalty for long stirring times so as to stir up as quickly as possible.
- Use machine learning optimised persistent currents as a starting point for superfluid instability investigations (i.e. the superfluid Kelvin-Helmholtz instability)

[1] G. Carleo et. al., *Rev. Mod. Phys.* **91**, 1539-0756 (2019).
[2] Q. Zhou, P. Tang, S. Liu, J. Pan, Q. Yan, and Shou-Cheng Zhang, *Rev. Mod. Phys.* **Proceedings of the National Academy of Sciences**, 0027-8424 (2018).
[3] S. Pilati and P. Pieri, *Scientific Reports* **9**, 2045-2322 (2019).
[4] A, J, Barker et. al., *Machine Learning: Science and Technology* **1**, 2632-2153 (2020).
[5] I. Nakamura et. al., *Opt. Expres Reports* **27**, 20435-20443 (2019)
[6] P. B. Wigley et. al., *Scientific Reports* **6**, 2045-2322 (2016).
[7] S. Pandey et. al., *Nature (London)* **570**, 1476-4687 (2019).
[8] M. Edwards, *Nature physics* **9**, 1745-2481 (2013).
[9] G. Gauthier et. al., *Optica* **3**, 1136-1143 (2016).

**Title:** Machine Learning Optimised Persistent Currents In BECs

**Candidate:** S. Simjanovski

**Abstract:**

Bose-Einstein condensates (BECs) are an ideal system for studying and controlling superfluid persistent currents [1]. A persistent current can be used as a matter-wave interferometer, allowing for highly sensitive measurements to be made on rotation, inertia or even gravity [1, 2]. Typically, persistent currents are generated through stirring of the condensate. Here, the use of machine learning to control and optimise the stirring process is considered experimentally. Two types of optimisation are considered: optimisation to a target flow velocity and maximisation of the same flow velocity. Both approaches attempt to remove spurious excitations due to the stirring by punishing them in the cost function. For the two cases explored, the learner successfully finds parameter sets which achieve the desired conditions in the persistent current.

[1] M. Edwards, *Nature physics* **9**, 1745-2481 (2013).

[2] S. Pandey et. al., *Nature (London)* **570**, 1476-4687 (2019).

# Multiple Populations of Globular Clusters: By Our Powers Combined

The University of Queensland Australia

Ellen Leitinger    A/Prof. Holger Baumgardt    Dr. Ivan Cabrera-Ziri    Dr. Michael Hilker

*The University of Queensland and European Southern Observatory, 2021*

## The Multiple Population Mystery

Most globular clusters in the Milky Way contain **multiple populations** of stars. The stars in each population exhibit variances in ages, chemical abundance spreads and kinematics.

Photometry can be used to show the distinction between multiple populations [1]:

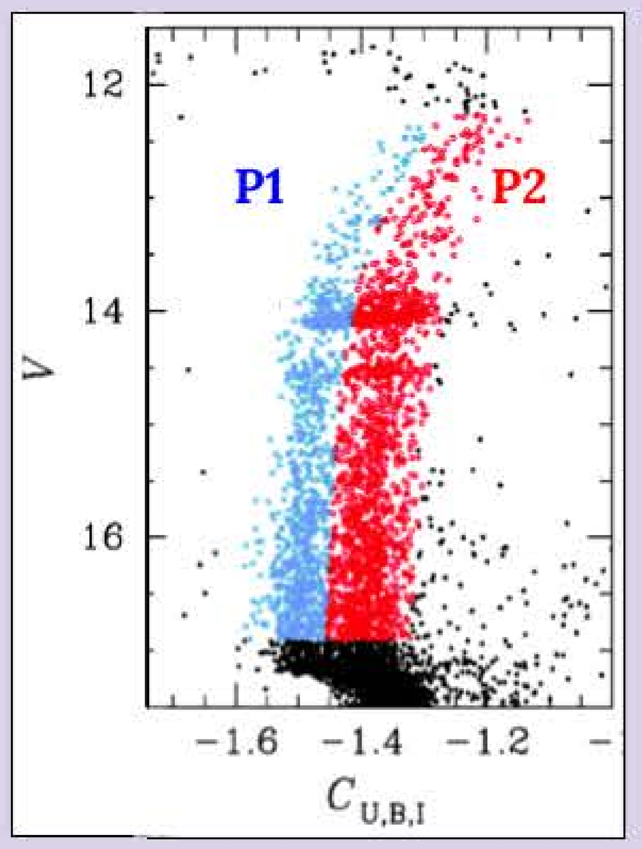


Most clusters contain a population with chemical abundance spreads consistent with the surrounding stars (P1) and at least one enriched population (P2). But the big question is: **How did they form?**

There are *many* theories, but so far no consensus.

**For now, our aim is to combine multiple data sets for dozens of clusters and perform a comprehensive analysis on the differences between populations.**

## How are Stars Split into Multiple Populations?

Colour-magnitude diagrams (CMDs) use different photometric bands to show the abundance variations between populations.

The focus of our analysis is on the Red Giant Branch (RGB) stars, so we use CMDs to clean the photometry of stars that don't belong to the cluster or the RGB.

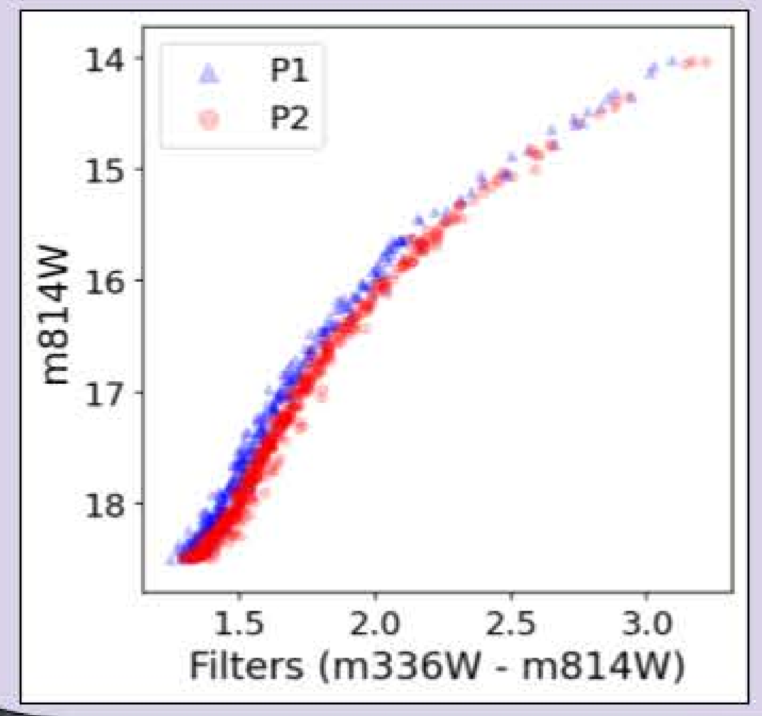


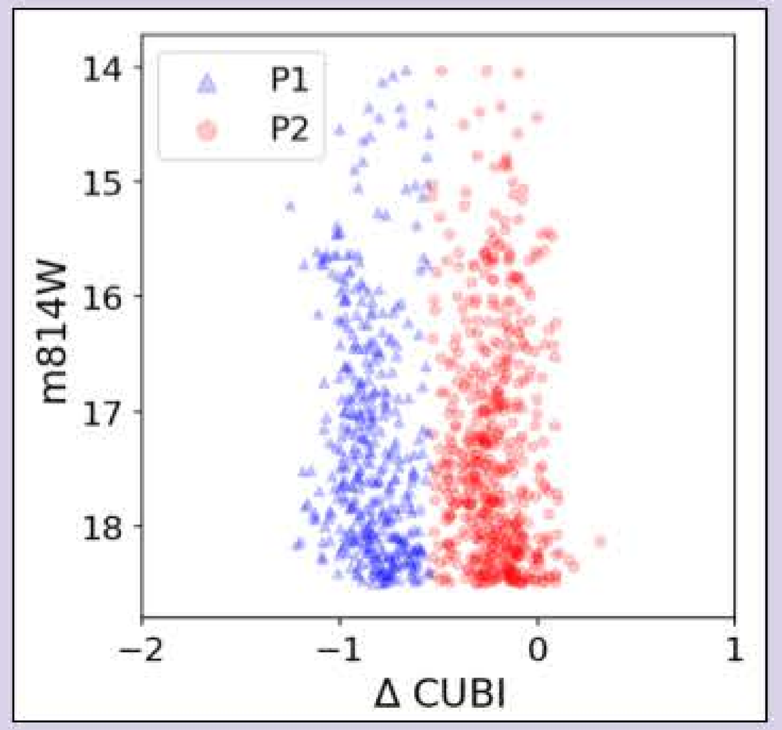


A special combination of photometric bands (CUBI) [2] transform the previous CMD of stars into a normalised Δ CUBI plot, which straightens out the RGB and clearly shows the split between the P1 and P2 populations.

The distribution of stars in the Δ CUBI plot are fit with Gaussian Mixture Models of varying degrees to find the most likely number of populations in a cluster.

Stars are assigned to a population based on their membership probability to each Gaussian.

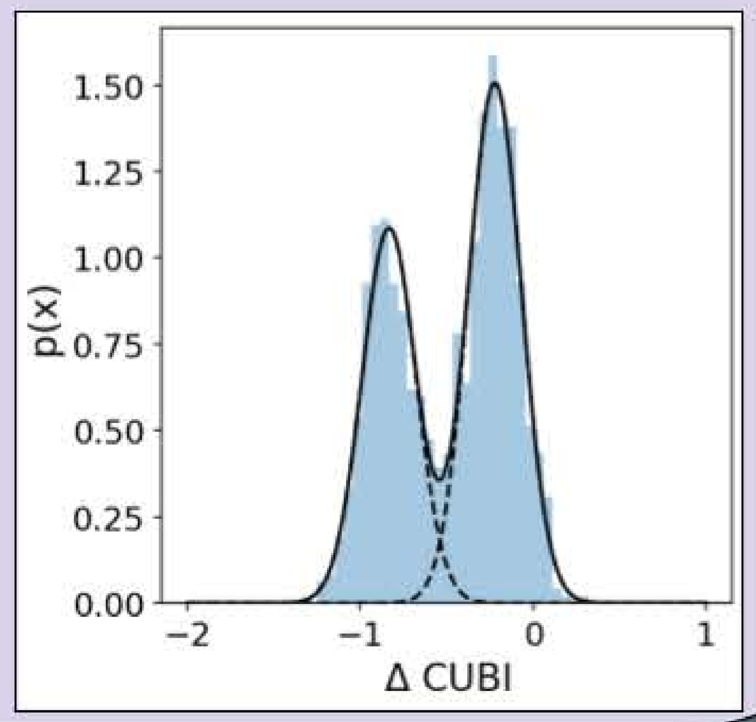


## We Need the Full Picture

The space-based photometry of the Hubble Space Telescope [2] shows only the densely concentrated inner stars of a globular cluster.

+

Stetson et al. [3] provides ground-based photometry that also includes outer stars, which are less densely concentrated.

=

By combining space-based *and* ground-based photometry, we can analyse all stars in a cluster.

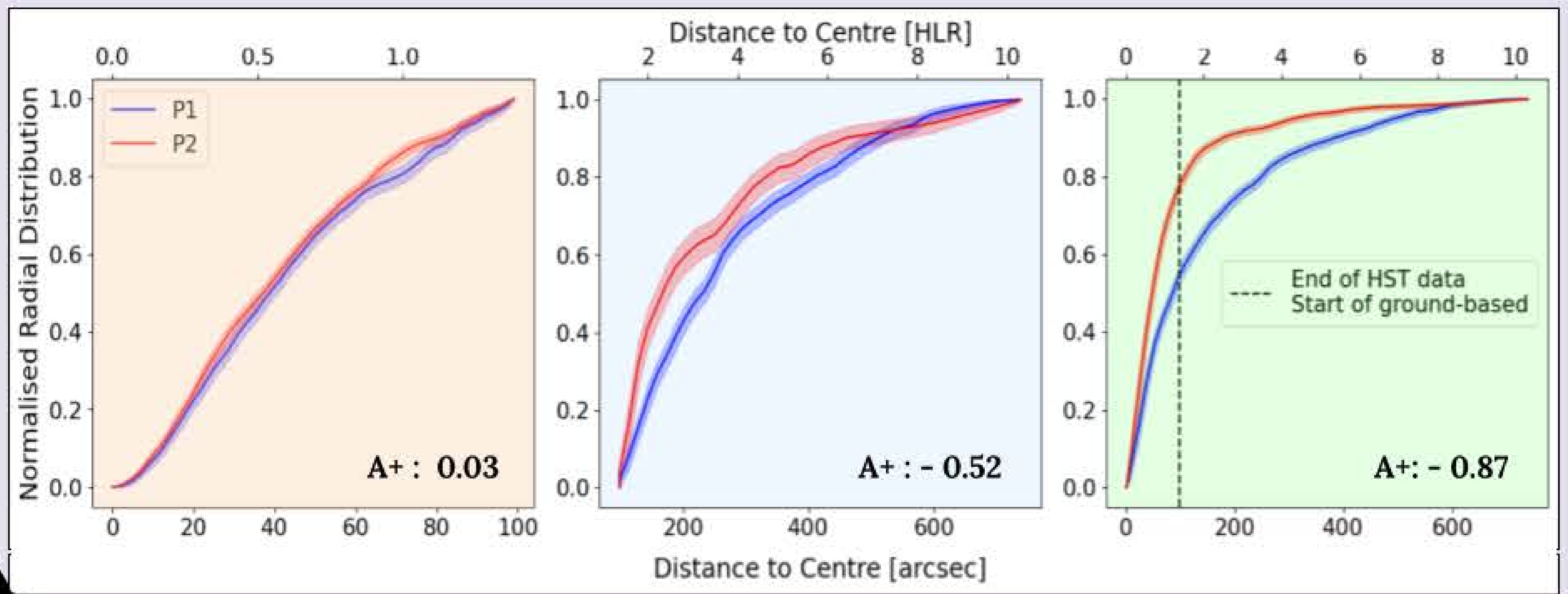


The normalised, cumulative radial distribution (A+) describes which population is centrally concentrated within a cluster.

**Positive A+**
P1 is in the centre

**Negative A+**
P2 is in the centre

**A+ close to zero**
The populations are well-mixed throughout the cluster

Focusing on the inner stars alone can give misleading results, as the differences between populations may only be apparent when the full cluster is analysed.

## Observing the Properties of Clusters

We analysed **28 globular clusters** using photometry and found a correlation between A+ and the ratio determining how much of a cluster's initial conditions are lost over time (relaxation time relative to age).

**Clusters which had not yet undergone significant dynamical mixing retained their initial conditions and were either P1 or P2 centrally concentrated.**

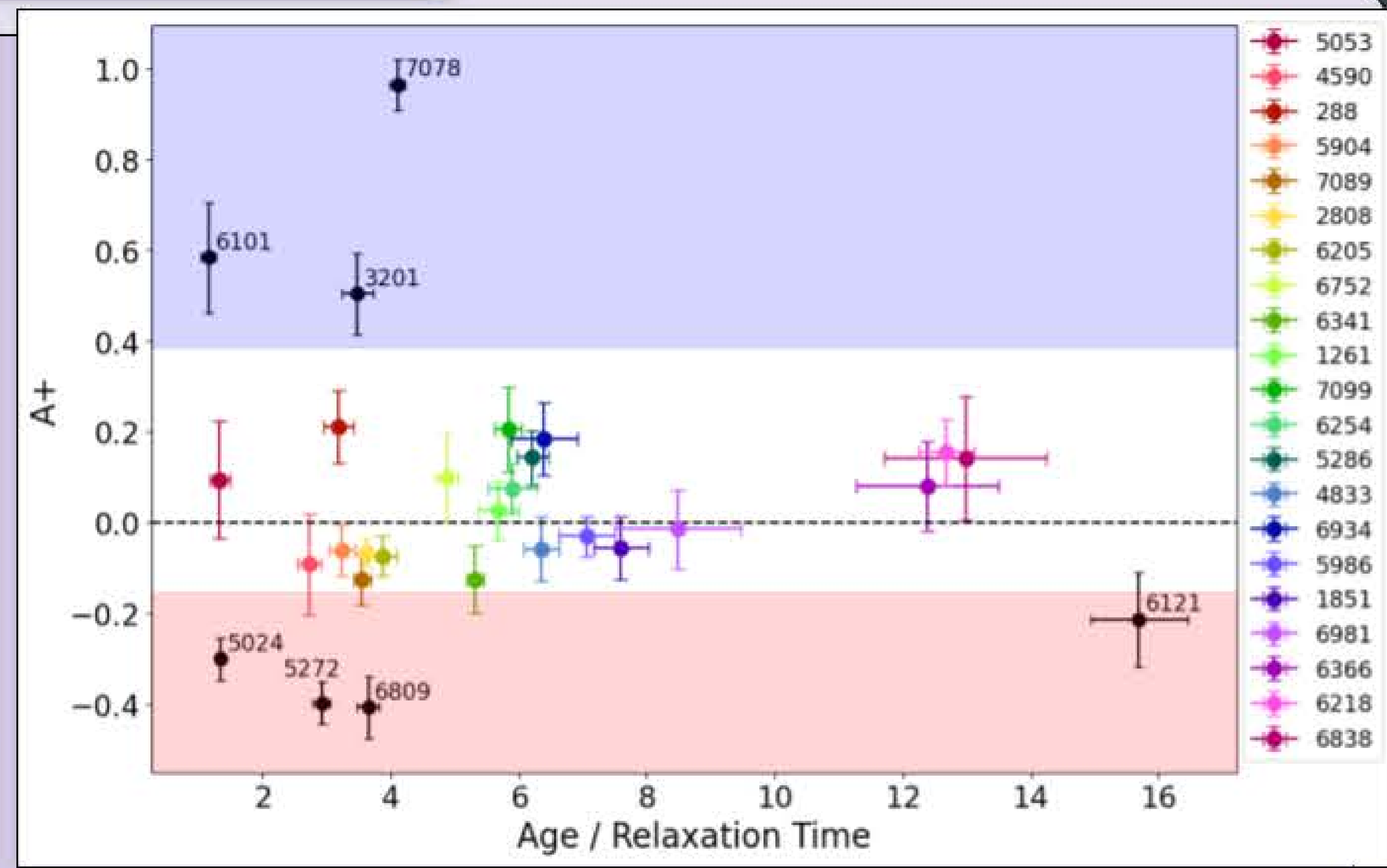


Investigating the A+ parameter as a function of mass loss also showed **clusters which retain a large fraction of their initial mass are also P1 or P2 centrally concentrated**. Future analysis into the kinematics, orbital parameters and spectroscopy of these 28 clusters will bring us closer to discovering the details of their initial conditions.

## Conclusion

**Space-based and ground-based photometry were successfully merged in order to analyse the full spatial extent of 28 globular clusters. This is important as properties of the stars in multiple populations can vary between the central and outer regions of a cluster. We found the clusters with lower mass loss and higher relative relaxation times retain their initial properties and are therefore key in determining the conditions of cluster formation.**

## References

[1] Milone et al. 2018 (arxiv: 1807.03511)
[2] Monelli et al. 2013 (arxiv: 1303.5187)
[3] Nardiello et al. 2018 (arxiv: 1809.04300) and Piotto et al. 2014 (arxiv: 1410.4564)
[4] Stetson et al. 2019 (arxiv: 1902.09925)

**Title:** Multiple Populations of Globular Clusters: By Our Powers Combined

**Candidate:** Ellen Leitinger

**Abstract:**

Globular clusters are relics of the early universe, containing some of the oldest stars known to astronomers and providing unique insight into the evolution of the universe. Recent research has focused on the mysteries of their formation and their peculiar chemical abundance patterns. To contribute to this, we combine space-based and ground-based photometry to homogeneously analyse the properties of the multiple populations of stars present in Galactic globular clusters. We study the full extent of each cluster from the centre to the outermost regions for a diverse sample of 28 clusters spanning a wide range of parameters. A comprehensive analysis of this kind has not previously been completed and future work aims to further incorporate available data sets to test the current theories on cluster formation.

# Nanomechanical computing

***Timothy Hirsch*** *(Phd Candidate, unconfirmed), Nicolas Mauranyapin, Erick Romero, Christopher Baker, Tina Jin, Glen Harris, Warwick Bowen*

Electronic circuits are ubiquitous but imperfect. They can be disabled by the ionising radiation found in outer space and nuclear plants. Additionally, as device dimensions shrink it is increasingly difficult to improve the basic efficiency of semiconductor logic.

We are developing an alternative *nanomechanical* computing architecture, which compared with electronics promises radiation hardness and the possibility of orders of magnitude lower energy cost per logic operation.

Previous architectures have connected mechanical components using electrical transducers, which lose the benefit of radiation hardness and reduce efficiency by a factor of $10^6$ [1]. We have avoided those problems by devising all-mechanical methods for transmission, connection, and logic.

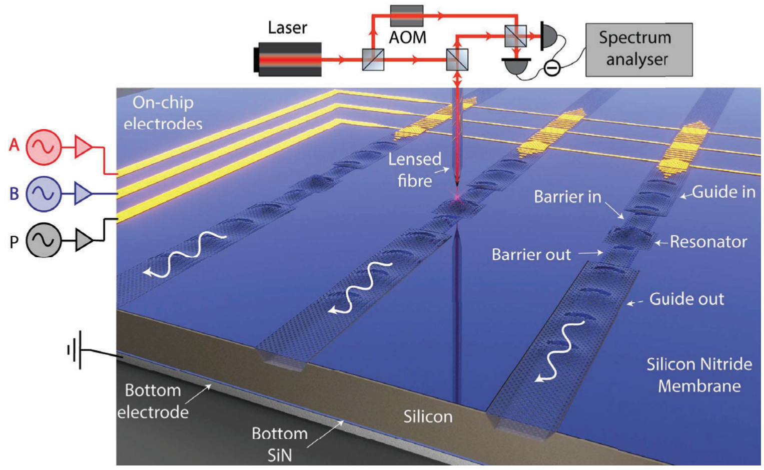


## Robust low-loss transmission

Transverse acoustic waves carry logical information. We confine them to suspended membrane waveguides made of silicon nitride [2].

Stress in the membranes increases the lossless tension energy, diluting the damping factor and reducing dissipation [3].

The finite width of the waveguides creates a single-mode frequency band (blue shaded area) where signals robustly propagate.

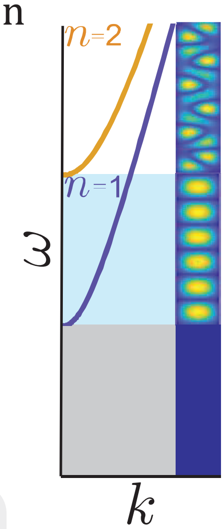


## All-acoustic connections

Previous methods for coupling circuit components used effective spring interactions, which introduced unwanted resonances that complicated the frequency response.

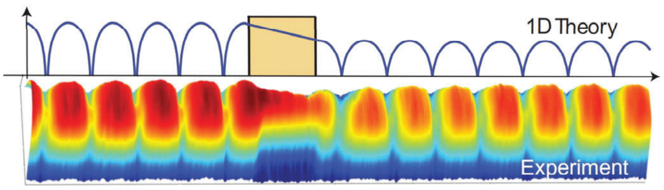


We instead couple components with zero-mode waveguides [4]. Virtual phonons tunnel across evanescently in the same fashion as quantum tunnelling.
Because the transmission is evanescent the couplers do not introduce resonances. Ours is the first scalable coupling method that avoids electrical transducers.

## Nonlinear logic

The equation of a vibrating string is well known: there is loss, and an elastic restoring force (Hooke's law). However, at large enough amplitudes the string will stretch, introducing a cubic *Duffing* term to the equation of motion.

$$m\ddot{u} + 2\Gamma\dot{u} + ku + \alpha u^3 = 0.$$

Because of this stretching Duffing nonlinearity our resonators are bistable when strongly driven near resonance: at the same frequency, they may oscillate at distinct high and low amplitudes. We use the two amplitudes to represent the logical '0' and '1'.

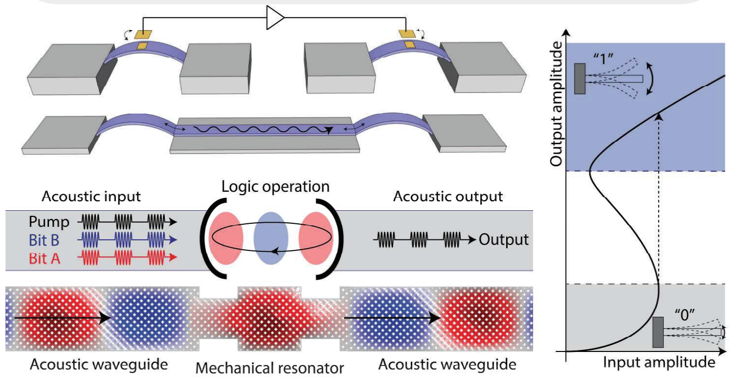


By pumping the resonator to one side of the hysteritic bistability we can set the resonator to 'jump up' or 'jump down' depending on the input acoustic signals, with an energy cost of only femtojoules.

Earlier this year we thus demonstrated a NAND gate in our architecture [5]. NAND gates are functionally complete, so this result implies nanomechanical logic can represent any truth table.

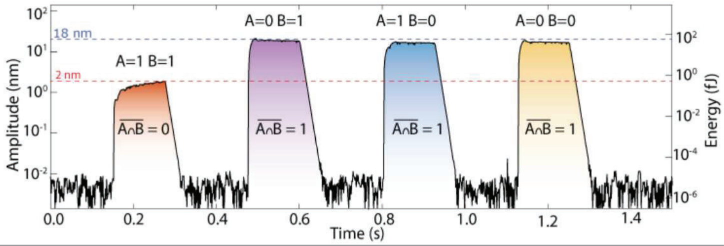


## What's next?

*Error-correcting memory:*
Momentum kicks, such as from high energy particles, could flip a mechanical bit. We propose the first nanomechanical error correcting memory, in the form of three coupled nonlinear oscillators [6]. Because of the nonlinear amplitude-dependent frequency shift, error correction is robust even when two oscillators are kicked.

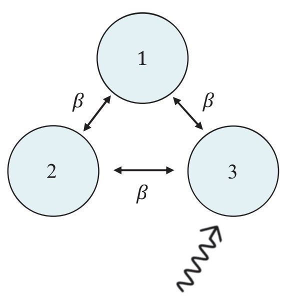

Momentum kick

*Solitons:*
Dispersion broadens pulses, limiting signal bandwidth. By balancing it against nonlinearity in our waveguides we aim to produce the first nanomechanical soliton. We are exploring two methods: engineering a phononic crystal structure to change the dispersion relationship, and introducing nonlinear electrostatic softening.

*Cascaded circuitry:*
We are currently fabricating complex logic circuits featuring half adders, full adders, and transistors. We are also testing new resonator geometries with far lower nonlinear threshold energies.

[1] Wenzler, J.-S., Dunn, T., Toffoli, T. & Mohanty, P. A Nanomechanical Fredkin Gate. Nano Lett. 14, 89–93 (2014).
[2] Romero, E. *et al.* Propagation and Imaging of Mechanical Waves in a Highly Stressed Single-Mode Acoustic Waveguide. Phys. Rev. Applied 11, 064035 (2019).
[3] Sementilli *et al.* Nanomechanical Dissipation and Strain Engineering. arXiv:2105.14946 (2021)
[4] Mauranyapin, N. P. *et al.* Tunneling of Transverse Acoustic Waves on a Silicon Chip. Phys. Rev. Applied 15, 054036 (2021)
[5] Romero, E. and Mauranyapin, N. P. *et al.* Scalable Nanomechanical Logic. In preparation.
[6] Jin *et al.* In preparation.

**Title:** Nanomechanical Computing

**Candidate:** Timothy Hirsch

**Abstract:**

Electronic circuits are ubiquitous but imperfect. They can be disabled by the ionising radiation found in outer space and nuclear plants. Additionally, as device dimensions shrink it is increasingly difficult to improve the basic efficiency of semiconductor logic. We are developing an alternative nanomechanical computing architecture, which compared with electronics promises radiation hardness and the possibility of orders of magnitude lower energy cost per logic operation. Previous architectures have connected mechanical components using electrical transducers, which lose the benefit of radiation hardness and reduce efficiency by a factor of 10^6. We have avoided those problems by devising all-mechanical methods for transmission, connection, and logic.

# Two-temperature estimation in the quantum regime: using Mach-Zehnder interferometer and quantum process framework

Harshit Verma , Magdalena Zych, Fabio Costa

h.verma@uq.edu.au

*ARC Centre of Excellence for engineered quantum systems (EQUS), School of Mathematics and Physics, University of Queensland, St Lucia 4072, QLD, Australia*

*School of Mathematics and Physics, University of Queensland, St Lucia 4072, QLD, Australia*

## INTRODUCTION

- Question: What does it mean to have a superposition of thermalizing quantum channels ?
- Approach:
  - Exert Q-ctrl over the state of a bath – prepare it in a superposition of purified Gibbs' state.
  - Exert Q-ctrl over the path of the probe, prepare it in a superposition where it goes through 2 different baths.
- Refined question: How effectively can we measure the temperature of the bath(s) in the above 2 approaches ?

## MULTIPARAMETER ESTIMATION & CR BOUND(S)

- How well can a parameter be estimated ?
- Density matrix – contains all the information we need (nonlinear fn. of parameter of interest).
- QFI: Mostly used in context of phase estimation – for e.g. in case of MZ interferometer:

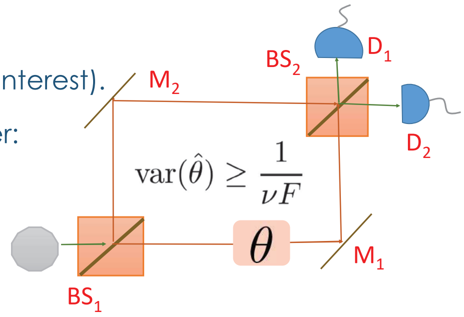


$$\mathrm{var}(\hat{\theta}) \geq \frac{1}{\nu F}$$

*ν – Repetitions of expt.*
*F – Q. Fisher Information*

Our scheme : State preparation of qubit(s) as probe(s) → Temperature(s) encoded through interaction with bath(s) → Measurement and estimation of temperature

### THERMALIZATION MODEL

Purified thermal bath constituted by 2 qubits:

$$|\theta^{\beta}\rangle \equiv \frac{e^{-E_0\beta/2}}{\sqrt{e^{-E_0\beta}+e^{-E_1\beta}}}|0,0\rangle + \frac{e^{-E_1\beta/2}}{\sqrt{e^{-E_0\beta}+e^{-E_1\beta}}}|1,1\rangle$$

$$T = 1/\beta$$

$$H_B = H_0 \otimes \mathbb{I}_2 + \mathbb{I}_2 \otimes H_0$$
$$H_0 = E_0|0\rangle\langle 0| + E_1|1\rangle\langle 1|$$

Interaction unitary (U):

$$U^{\eta}_{PB} = \begin{pmatrix} 1 & 0 & 0 & 0 \\ 0 & \sqrt{1-\eta} & \sqrt{\eta} & 0 \\ 0 & -\sqrt{\eta} & \sqrt{1-\eta} & 0 \\ 0 & 0 & 0 & 1 \end{pmatrix}$$

Multiparameter CR bound :

$$\boxed{\mathrm{Cov}(\vec{T}) \geq \frac{\mathcal{Q}_T^{-1}}{\nu}}$$

Bounds derived from the above matrix inequality :

$$\mathrm{Var}(T_1) \geq \frac{\mathcal{Q}_{T_2T_2}}{\nu \det(\mathcal{Q}_{\mathcal{T}})}$$

$$\mathrm{Var}(T_2) \geq \frac{\mathcal{Q}_{T_1T_1}}{\nu \det(\mathcal{Q}_{\mathcal{T}})}$$

$$\left(\mathrm{Var}(T_1) - \frac{\mathcal{Q}_{T_2T_2}}{\nu \det(\mathcal{Q}_{\mathcal{T}})}\right)\left(\mathrm{Var}(T_2) - \frac{\mathcal{Q}_{T_1T_1}}{\nu \det(\mathcal{Q}_{\mathcal{T}})}\right) \geq \left[\mathrm{Cov}(T_1,T_2) + \frac{\mathcal{Q}_{T_1T_2}}{\nu \det(\mathcal{Q}_{\mathcal{T}})}\right]^2$$

## NUMERICAL RESULTS FOR THE MACH ZEHNDER SETUP

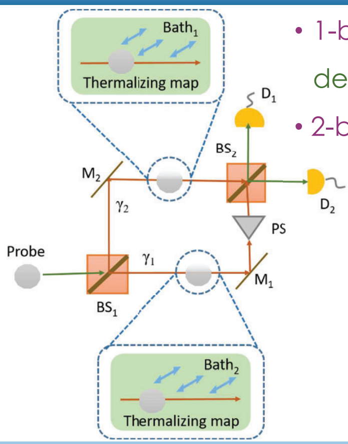


- 1-bath: The state of the (thermal) bath depends on the control (path).
- 2-bath: Two independent baths on the paths.

For a single qubit as a probe:

- 1-bath/ 2-bath : |QFIM| = 0 ⇒ Bounds cannot be obtained.
- For a two- qubit probe, |QFIM| ≠ 0 (generally).

$\rho_{\text{in}} = |0\rangle\langle 0| \otimes |0\rangle\langle 0|$   Φ = π/2, ν = 100

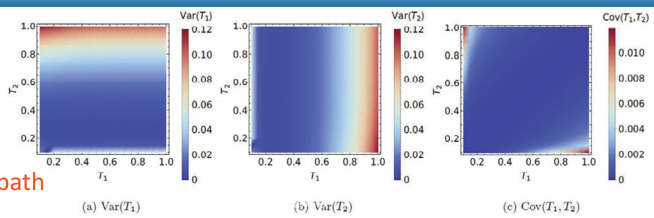

1 – bath

(a) Var($T_1$)   (b) Var($T_2$)   (c) Cov($T_1$, $T_2$)

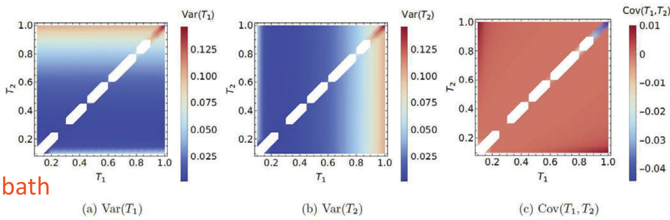

2 – bath

(a) Var($T_1$)   (b) Var($T_2$)   (c) Cov($T_1$, $T_2$)

## NUMERICAL RESULTS FOR THE QUANTUM SWITCH BASED SETUP

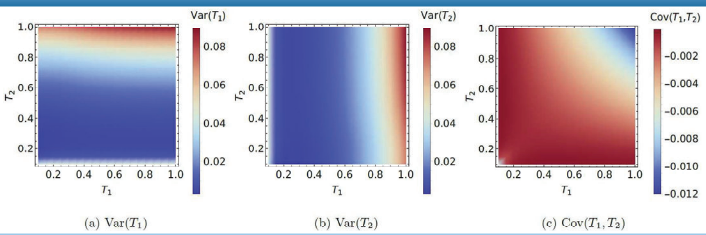

(a) Var($T_1$)   (b) Var($T_2$)   (c) Cov($T_1$, $T_2$)

- Indefinite causal order via. Q - Ctrl over order of application of 2 thermalizing channels.

$\rho_{\text{in}} = |0\rangle\langle 0| \otimes |+\rangle\langle +|$   ν = 100

*$\mathcal{A}_1, \mathcal{A}_2$: Quantum channels thermalizing to distinct temperatures.*

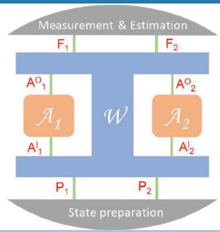


## CONCLUSIONS

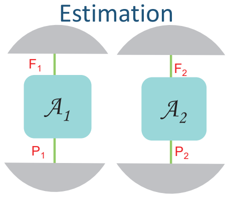


- Mach-Zehnder interferometer can be used for the task of estimating 2 temperatures, with 2 qubits as a probe.
- Qualitatively similar results for other setups based on quantum processes.
- Parallel scheme with simultaneous measurement of two temperatures using two independent probes outperforms all the others.

### REFERENCES

[1] Araújo, M., Feix, A., Navascués, M., & Brukner, C. *A purification postulate for quantum mechanics with indefinite causal order. Quantum*, 1, 1–13 (2017).

[2] Oi, D. K. L. *Interference of Quantum channels. Phys. Rev. Lett.*, 91(6), 67902 (2003).

[3] Liu, J., Yuan, H., Lu, X.-M., & Wang, X. *Quantum Fisher Information Matrix and Multiparameter Estimation. Journal of Physics A: Mathematical and Theoretical*, 53(2), 23001 (2019).

[4] Mukhopadhyay, C., Gupta, M. K., & Pati, A. K., *Superposition of causal order as a metrological resource for quantum thermometry. arXiv:1812.07508v1 (2018).*

**Title:** Two-temperature estimation in the quantum regime: using Mach-Zehnder interferometer and quantum process framework

**Candidate:** Harshit Verma


**Abstract:**

There has been a recent interest in leveraging quantum control over the evolution of systems to demonstrate advantages in various thermodynamical and communication tasks. Many setups used for such tasks rely on the quantum SWITCH, which allows for indefiniteness in the order of application of quantum channels. The SWITCH belongs to the broader class of quantum processes - essentially higher order linear transformations from quantum maps to quantum maps. If considered with thermalizing quantum channels (corresponding to two distinct temperatures), the quantum process framework and interferometric scheme with parallel application of channels constitute an interesting scenario with the possibility of two-temperature estimation. We investigate this prospect in setups based on various types of quantum processes and affirm their utility for this task. We provide the bounds on variances of the temperatures (obtained through multi-parameter Cramer-Rao bounds), which we also find to be attainable. Our results demonstrate that there is no significant advantage offered in using quantum processes, if compared with the case wherein the two temperatures are estimated independently.

# Overcoming the repeaterless bound in continuous-variable quantum communication without quantum memories

Matthew S. Winnel, Joshua J. Guanzon, Nedasadat Hosseinidehaj, Timothy C. Ralph

Centre for Quantum Computation and Communication Technology,
School of Mathematics and Physics, University of Queensland, St Lucia, Queensland 4072, Australia

## 1. Introduction

- Quantum communication is the art of transferring quantum states from one location to another.
- Important applications include secret communication, quantum teleportation, and distributed quantum computing.
- One of the main problems is how to achieve high rates at long distances.
- The repeaterless bound is the highest rate achievable by any point-to-point protocol and scales like the transmissivity of the channel at large distances. Quantum repeaters are required to overcome the repeaterless bound, assumed to be untrusted and can be operated by the malicious eavesdropper (Eve).
- Before our work, no simple and practical repeater protocol was known for continuous-variable systems, where the quantum information is encoded in the quadratures of the light (the real and imaginary parts of the complex amplitude).

## 2. Aim

- to introduce a simple and practical continuous-variable quantum key distribution protocol for overcoming the repeaterless bound

## 3. Noiseless linear amplification

- Noiseless linear amplification can be performed probabilistically using a linear-optics device called a quantum scissor.
- We found that the quantum scissor is tolerant to loss inside the device which means the probability of success can be improved. Remarkably, this means that the quantum scissor can overcome the repeaterless bound, demonstrating that it is working as an effective quantum repeater.
- The gain of the amplifier is set by the transmissivity of the beam-splitters and the location of the relay between the trusted parties, Alice and Bob.

## 4. Security

- A lower bound on the asymptotic secret key rate is [1]

$$K = P(\beta_{\text{rec}} I_{AB} - \chi_{EB}),$$

where $I_{AB}$ is the classical mutual information between Alice and Bob, $\beta_{\text{rec}}$ is the reconciliation efficiency (we set it to $95\%$), $\chi_{EB}$ is Eve's maximal information [2], and $P$ is the probability of successful operation of the repeater.

- We assume ambient conditions (thermal-loss channel) to simulate parameters observed in an experiment. Note that no assumption on the channel is required in an experiment for asymptotic security and the relay can be operated by Eve.

## 5. Our continuous-variable quantum-repeater protocol

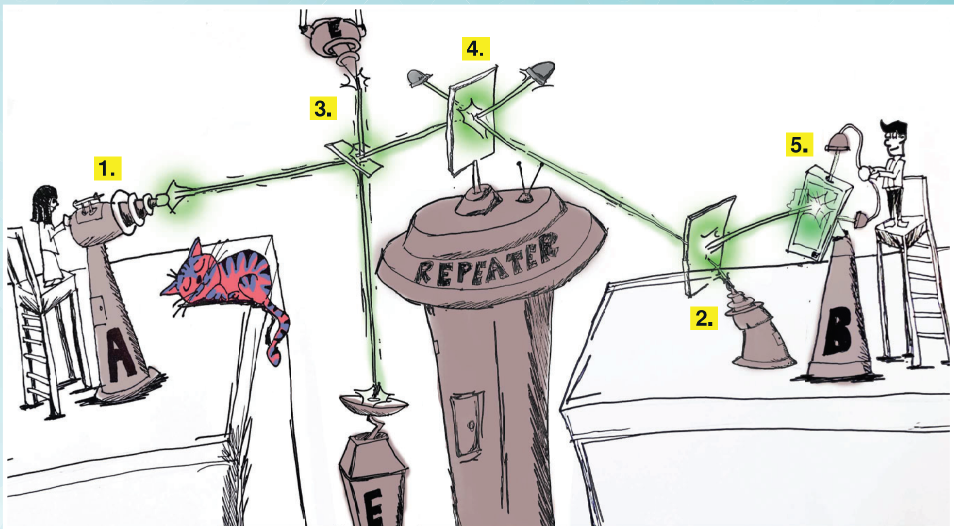


**1.** Alice's input

Alice (A) chooses a coherent state at random from a two-dimensional Gaussian distribution and forwards it to the repeater.

**2.** Bob's entanglement resource

Bob (B) prepares an entangled-resource state by combining a single photon with vacuum on a beamsplitter. He sends one output mode towards the repeater and keeps the other mode.

**3.** Eve

We assume that all-powerful Eve (E) controls the channel and the repeater station. In the illustration, she is shown attacking Alice's signal as it travels to the repeater.

**4.** Repeater station

The repeater interferes the modes on a beamsplitter and performs photon-number-resolving detection. A single click at exactly one of the detectors teleports and amplifies the state Alice sent across the second half of the channel to Bob.

**5.** Bob's measurement

Bob measures his remaining mode with heterodyne detection.

### Quantum-communication rate

The probability of success of the repeater scales like the square root of the transmissivity of the total distance, thus, the repeater improves the rate-distance scaling and can overcome the repeaterless bound.

## Acknowledgements

We thank Dave Winnel for the illustration. This research was supported by the Australian Government Department of Defence and by the Australian Research Council (ARC) under the Centre of Excellence for Quantum Computation and Communication Technology.

## References

[1] I. Devetak and A. Winter, Proceedings of the Royal Society A: Mathematical, Physical and Engineering Sciences **461**, 207 (2005).

[2] A. S. Holevo, Problems Inform. Transmission **9**, 3 (1973).

[3] S. Pirandola, R. Laurenza, C. Ottaviani, and L. Banchi, Nature Communications **8**, 10.1038/ncomms15043 (2017).

[4] S. Pirandola, Communications Physics **2**, 10.1038/s42005-019-0147-3 (2019).

## 6. Secret key rate

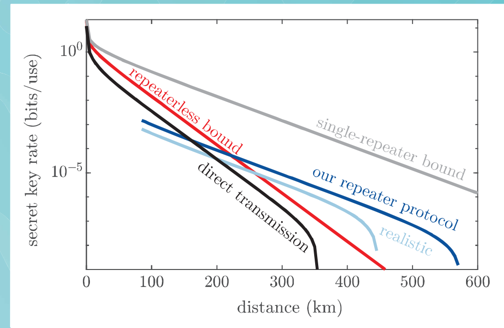


Fig. 1: Secret key rate of our continuous-variable quantum key distribution protocol based on coherent states and heterodyne detection versus the total distance between Alice and Bob assuming standard optical fibre (0.2 dB/km) and some excess noise. The strength of Alice's EPR state is $\chi = 0.4$ ($V_A = 0.38$ in the PM version). For the realistic implementation (light blue), we assume $75\%$ single-photon source and single-photon detector efficiencies and $10^{-8}$ dark-count rate probability, whilst these are assumed perfect for ideal (dark blue). We plot direct transmission for optimised modulation variance and with excess noise. We also plot the (pure-loss) point-to-point repeaterless PLOB bound [3] and the single-repeater bound [4]. Note that a protocol based on squeezed states and homodyne detection can increase the key rate.

## 7. Conclusion

- We introduced a simple continuous-variable protocol which can beat the repeaterless bound using existing technology.
- The protocol is tolerant to some excess noise and imperfections.
- The protocol can be extended into a chain of quantum repeaters using quantum memories, requiring just half the number of resources as previous continuous-variable protocols.
- Higher-order scissors can be used to loss-tolerantly amplify larger input states (at a diminished probability of success).

Future work:

- An open question is how to approach the single-repeater bound (excitingly, this is soon to be published by the authors).
- to use our protocol to reliably connect multiple trusted users
- to include finite-size effects

Our preprint appears here: https://arxiv.org/abs/2105.03586

## Contact

Matthew Winnel
matthew.winnel@uqconnect.edu.au

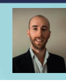

CENTRE FOR QUANTUM COMPUTATION & COMMUNICATION TECHNOLOGY
AUSTRALIAN RESEARCH COUNCIL CENTRE OF EXCELLENCE

Australian Government
Australian Research Council

The University of Queensland
AUSTRALIA

**Title:** Overcoming the repeaterless bound in continuous-variable quantum communication without quantum memories

**Candidate:** Matthew Winnel

**Abstract:**

Quantum communication is the art of transferring quantum states from one location to another. One of the main problems is how to achieve high rates at long distances. Quantum repeaters are necessary to overcome the repeaterless bound which sets the fundamental rate-distance limit of repeaterless communications. Unfortunately, quantum repeaters are often complicated devices and not very practical. On this poster, we illustrate our simple continuous-variable quantum key distribution protocol for overcoming the repeaterless bound. The protocol can be implemented with existing technology as it requires no quantum memories and is robust to experimental noise and imperfections. We expect it to be a fundamental building block for larger quantum networks and the quantum internet.

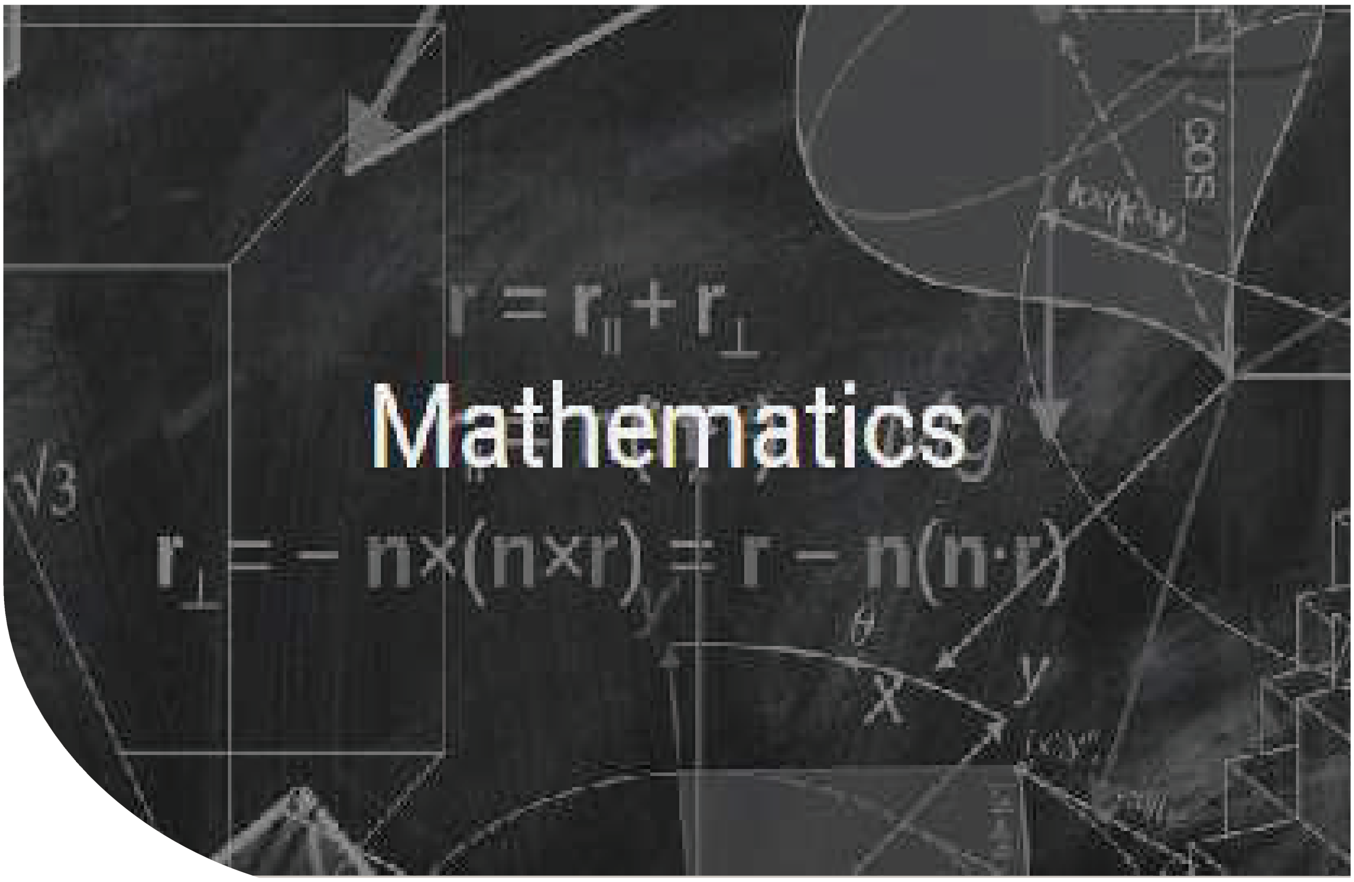
Mathematics
$r = r_{\parallel} + r_{\perp}$
$r_{\perp} = - n \times (n \times r) = r - n(n \cdot r)$

# Learn to Pickup and Deliver

Lucas Sippel
School of Mathematics and Physics
lucas.sippel@uqconnect.edu.au

Advisors: Dr Michael Forbes & Dr Slava Vaisman

The University Of Queensland
AUSTRALIA

## The Pickup and Delivery Problem with Time Windows (PDPTW)

- Vehicles with limited capacity, ***q***.
- Have ***n*** requests each with a pickup vertex and delivery vertex in directed complete graph G. A pickup and delivery must be completed in the same route.
- Each vertex has a time window and demand for vehicle space.
- Calculate a set of routes which covers all requests once, has the minimum number of vehicles and the minimum total travel time.

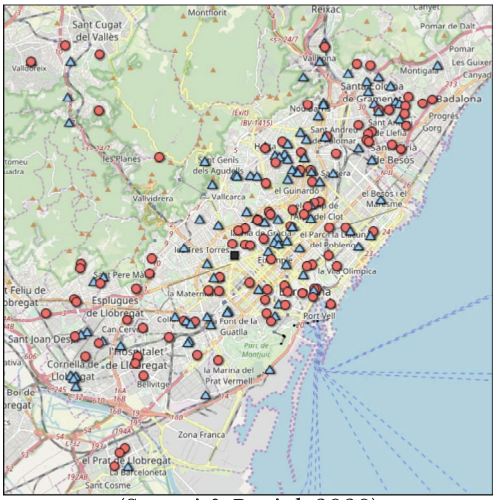

(Sartori & Buriol, 2020)

## Fragments

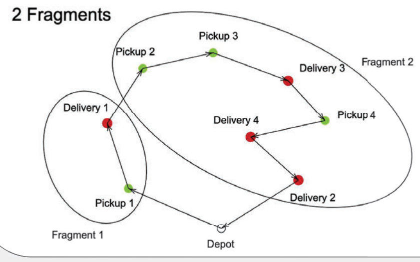


Satisfies **time windows** and vehicle **capacity**.

Maintains **positive load.**

**Far fewer** fragments than routes.

## Solution Technique

1. Make timed copies of **fragments** (arrows) connecting timed copies of **vertices** (circles).
2. Add **arcs** (dotted).
3. Use a **network flow integer program** to construct minimum cost paths through the time discretised network, ensuring:
   a. Each pickup is **covered** by a timed fragment.
   b. At each timed vertex, **binary flow is conserved.**

(Alyasiry et al, 2019)

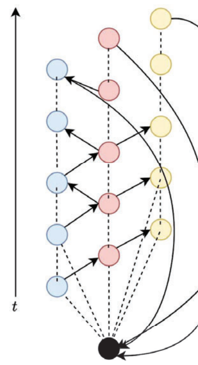


## Imitating Optimal Extensions

Large ***q*** or ***n*** or wide time windows. → Intractable number of fragments.

We restrict extensions to new nodes from partial fragments by defining ordinal function *d* with learnable parameters $a_1$ and $a_2$:

Waiting time upon arrival at j

$$d(i,j,t^*,\bar{O};\underline{a}) = a_1 \cdot t_{ij} + a_2 \cdot w(i,j,t^*) + (1-a_1-a_2)\cdot c(\bar{O},j)$$

Travel time to j

Minimum distance from delivery of j to an onboard delivery

Only take the top **k** feasible extensions.

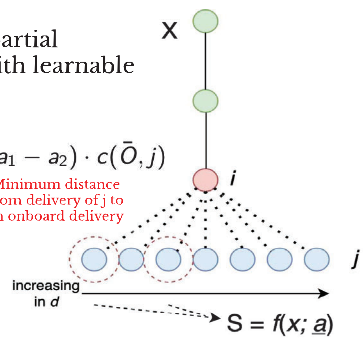


Collect optimal partial fragment and extension pairs $\{(X_k, j_k)\}_{k=1,\ldots,n}$ from small PDPTW instances. Find $a_1$ and $a_2$ minimising:

$$l(\underline{a}; \{(X_k, j_k)\}_{k=1}^{n}) = n - \sum_{k=1}^{n} \mathbb{I}_{j_k \in f(X_k;\underline{a})}$$

**80.3%** test set accuracy on a class of New York City taxi instances (k = 2). With on average **6 feasible extensions**, the model improves upon picking **random extensions by approximately 47%**.

## Results

The set of fragments is initialised using learned extensions. The fragment pool is improved via delayed column generation. The integer program is solved on the augmented set of fragments.

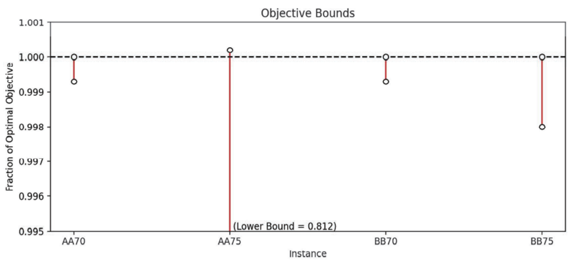


*Initial lower bound (bottom points) and best solution found (upper points)*

| $\lvert F\rvert$ Prop. | Solve Time (s) | Exact Solve Times (s) |
|---|---|---|
| 0.025 | 103.6 | 438.2 |
| 0.028 | 88.6 | 6442.4 |
| 0.097 | 59.0 | 418.1 |
| 0.073 | 217.0 | *1055.3 |

*Columns from left to right are: proportion of total fragments considered, time to prove best solution possible, and best exact solution time in the literature (Baldacci et al, 2011).*

## References

Alyasiry, A. M., Forbes, M., & Bulmer, M. (2019). An Exact Algorithm for the Pickup and Delivery Problem with Time Windows and Last-in-First-out Loading. Transportation science, 53(6), 1695-1705. doi:10.1287/trsc.2019.0905

Baldacci, R., Bartolini, E., & Mingozzi, A. (2011). An Exact Algorithm for the Pickup and Delivery Problem with Time Windows. Operations research, 59(2), 414-426. doi:10.1287/opre.1100.0881

Sartori, C. S., & Buriol, L. S. (2020). A study on the pickup and delivery problem with time windows: Matheuristics and new instances. Computers & operations research, 124, 105065. doi:10.1016/j.cor.2020.105065

**Title:** Learn to Pickup and Deliver

**Candidate:** Lucas Sippel


**Abstract:**

Pickup and delivery problems (PDPs) are applicable in many situations such as optimal movement of cargo, air lifting of troops, and bus or ship routing. Recently, fragment based solution techniques have been adopted for PDPs. In these techniques, paths through a network (fragments) are exhaustively enumerated and used to construct vehicle routes. As problem instances become larger and less constrained, the number of enumerated fragments becomes intractable which causes computer memory and solve time issues. By using supervised ma-chine learning models to reduce the fragments considered, it is possible to obtain near optimal solutions with less time and computational resources. This machine learning based restriction has shown promising results for the Pickup and Delivery Problem with Time Windows, a common PDP found in the literature.

# Perfect 1-Factorisations of Complete Uniform Hypergraphs

Jeremy Mitchell

Supervisors: Sara Herke | Barbara Maenhaut

## 1-Factorisations and Perfect 1-Factorisations of Graphs

A 1-regular spanning subgraph of a graph is *1-factor*. A decomposition of a graph $G$ into $\alpha$ edge-disjoint 1-factors is a *1-factorisation* of $G$, often denoted by $\mathcal{F} = \{F_1, \ldots, F_\alpha\}$.

### Perfect 1-Factorisations of Graphs

Let $\mathcal{F}$ be a 1-factorisation of a graph $G$. $\mathcal{F}$ is said to be a *perfect 1-factorisation* (P1F) of $G$ if it satisfies the following three equivalent conditions:

1. The union of each pair of 1-factors of $\mathcal{F}$ is isomorphic to some connected subgraph $H$.
2. The union of each pair of 1-factors of $\mathcal{F}$ is a Hamilton cycle.
3. The union of each pair of 1-factors of $\mathcal{F}$ is connected.

Figure 1: A Perfect 1-Factorisation of $K_6$

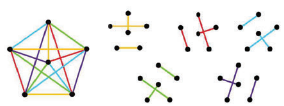

Figure 2: Union of Pairs of 1-Factors of P1F of $K_6$

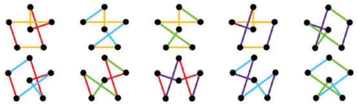

## 1-Factorisations of Hypergraphs

A hypergraph is a generalisation of a graph; formally a hypergraph is a pair $(X, E)$ where $X$ is a set of vertices and $E$ is a set of subsets of vertices of $X$ which are called *edges*. The generalisation of a 1-factorisation is very natural; a 1-regular spanning subhypergraph of a hypergraph $\mathcal{H}$ is known as a 1-factor. If $\mathcal{H}$ can be decomposed into edge-disjoint 1-factors, that decomposition is called a *1-factorisation* of $\mathcal{H}$. The hypergraph on $n$ vertices whose edge set is the set of all $k$-sets of vertices is called the *complete $k$-uniform hypergraph* on $n$ vertices, denoted by $K_n^k$.

### Generalisations of Perfect 1-Factorisations

Presently, there are no generalisations of P1Fs in the hypergraph setting. We propose three different generalisations, one for each of the equivalent conditions which define perfect 1-factorisations of graphs:

1. *Perfect 1-Factorisations* (P1Fs),
2. *Hamilton Berge 1-Factorisations* (HB1Fs),
3. *Connected 1-Factorisations* (C1Fs).

## Perfect 1-Factorisations of Complete $k$-Uniform Hypergraphs

### P1Fs of Hypergraphs

A 1-factorisation of a hypergraph $\mathcal{H}$ is a *perfect 1-factorisation* (P1F) if the union of each pair of distinct 1-factors is isomorphic to the same connected hypergraph.

### Existence of P1Fs of $K_n^k$

**Theorem**

P1Fs of $K_n^k$ do not exist for $k \geq 4$.

**Lemma**

There exist P1Fs of $K_3^3$, $K_6^3$, and $K_9^3$. Moreover, each of these P1Fs is unique up to isomorphism.

Figure 3: Any two 1-factors of a P1F of $K_n^3$ will have 2 pairs of vertices that appear in two edges together.

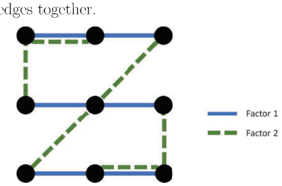


### Building Biplanes with P1Fs of $K_{3n}^3$

Building on work by Husain [4], we can build biplanes using P1Fs of $K_{3n}^3$. Biplanes are a well-studied class of designs.

**Lemma**

Let $\mathcal{F} = \{F_1, F_2, \ldots, F_{\binom{3n-1}{2}}\}$ be a P1F of $K_n^3$. Consider the design $\mathcal{D} = (\mathcal{V}, \mathcal{B})$ constructed in the following way:

- Let $V = V(K_{3n}^3) \cup \{F_1, F_2, \ldots, F_{\binom{3n-1}{2}}\}$.
- Let $B_0 = V(K_{3n}^3)$.
- For every unordered pair of vertices of $K_{3n}^3$, $x, y$, let
$$B_{xy} = \{x, y\} \cup \{F_i | \exists e \in F_i \quad s.t. \quad x, y \in e\}.$$
- Let $\mathcal{B} = B_0 \cup \bigcup_{xy} B_{xy}$.
$\mathcal{D}$ is a symmetric $\left(\binom{3n}{2} + 1, 3n, 2\right)$-design.

Thus, P1Fs of $K_{3n}^3$ can be ruled out when the parameters of a symmetric $\left(\binom{3n}{2} + 1, 3n, 2\right)$-design are not admissible.

**Lemma**

If there exists a P1F of $K_n^3$ where $n \leq 30$ then
$$n \in \{3, 6, 9, 18, 21, 27\}.$$

## Hamilton Berge 1-Factorisations of Complete $k$-uniform Hypergraphs

### Hamilton Berge Cycles of Hypergraphs

A *Berge cycle* in a hypergraph $\mathcal{H} = (V, E)$ is an alternating sequence
$$(v_1, e_1, v_2, e_2, \ldots, v_m, e_m)$$
of distinct vertices $v_i \in V$ and distinct edges $e_i \in E$, where $e_i$ contains $v_i$ and $v_{i+1}$ for each $i \in \{1, 2, \ldots, m\}$ and $e_m$ contains $v_m$ and $v_1$. A Berge cycle is a *Hamilton Berge cycle* of a hypergraph $\mathcal{H}$ if $\{v_1, \ldots, v_m\}$ is the vertex set of $\mathcal{H}$, and each $e_i$ is a distinct edge of $\mathcal{H}$.

We note that a hypergraph $\mathcal{H}$ has a Hamilton Berge cycle if and only if the incidence graph of $\mathcal{H}$ has a Hamilton cycle.

### HB1Fs of Hypergraphs

A 1-factorisation of a $k$-uniform hypergraph, $\mathcal{H}$, is called a *Hamilton Berge 1-Factorisation* if the union of each $k$-set of 1-factors of the 1-factorisation has a Hamilton Berge cycle.

Figure 4: The hypergraph from the union of three 1-factors of a 1-factorisation of $K_9^3$ and its incidence graph.

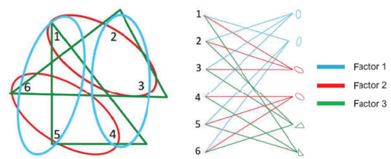


### Existence of HB1Fs of $K_n^k$

**Lemma**

The unique 1-factorisation of $K_{2k}^k$ is a HB1F.

**Conjecture**

All 1-factorisations of $K_{3k}^k$ are HB1Fs.

When viewing the above in terms of incidence graphs, we see that it is a special case of a famous conjecture by Häggkvist [3].

**Conjecture [3]**

All 2-connected $k$-regular bipartite graphs on $6k$ or fewer vertices contains a Hamilton cycle.

**Open Problem**

Does $K_n^k$ admit a HB1F for all $3 \leq k \leq \frac{n}{2}$ where $k|n$?

## Connected 1-Factorisations

### C1Fs of Hypergraphs

A 1-factorisation of a hypergraph $\mathcal{H}$ is a *connected 1-factorisation* (C1F) if the union of each pair of distinct 1-factors forms a connected hypergraph.

### Existence of C1Fs of $K_n^k$

**Lemma**

The unique 1-factorisation of $K_{2k}^k$ is a C1F.

**Lemma**

All 1-factorisations of $K_{3k}^k$ are C1Fs.

**Lemma**

For $\ell \geq 4$, there exists a 1-factorisation of $K_{\ell k}^k$ that is not a C1F.

**Open Problem**

Does $K_{\ell k}^k$ admit a C1F for all $\ell \geq 3$?

### Overview of Existence Results

Table 1: Several small of $k$ and $n$ and some known constructions of 1-factorisations of $K_n^k$ that are P1Fs, HB1Fs, or C1Fs.

| $n$ | $k$ | P1F | HB1F | C1F |
|---|---|---|---|---|
| 6 | 3 | All | All | All |
| 9 | 3 | [2] | All | All |
| 12 | 3 | ? | [1],[2] | [2] |
| $> 12$ | $\geq 3$ | ? | ? | ? |

### References

[1] T Beth. Algebraishce auflögsalorithmen für einige unendliche familien von 3-designs. *Le Matematiche*, 29:105–135, 1974.

[2] Hu Ye Chen and Zai Ping Lu. Symmetric factorizations of the complete uniform hypergraph. *Journal of Algebraic Combinatorics*, 46(2):475–497, 2017.

[3] R Häggkvist. Unsolved problems. In *Proc. Fifth Hungarian Colloq. Comb.* Keszthely, 1976.

[4] QM Husain. On the totality of the solutions for the symmetrial incomplete block designs: λ= 2, k= 5 or 6. *Sankhyā: The Indian Journal of Statistics*, pages 204–208, 1945.

**Title:** Perfect 1-Factorisations of Complete Uniform Hypergraphs
**Candidate:** Jeremy Mitchell

**Abstract:**
A 1-factorisation of a graph is called perfect if it satisfies the following equivalent conditions:

The union of each pair of 1-factors is isomorphic to the same connected subgraph .
The union of each pair of 1-factors is connected.
The union of each pair of 1-factors is a Hamilton cycle.
Based on these conditions we define three generalisations of perfect 1-factorisations of graphs to the context of hypergraphs, called perfect 1-factorisations, connected 1-factorisations, and Hamilton Berge 1-factorisations respectively and we ask whether the complete uniform hypergraph  admits such 1-factorisations. We show that perfect 1-factorisations of complete -uniform hypergraphs can only exist when , and when they exist, they can be used to construct biplanes. We also show that all 1-factorisations of and are connected 1-factorisations, and prove the existence of non-connected 1-factorisations of  for any . We prove that all 1-factorisations of  are Hamilton Berge 1-factorisations and demonstrate a strong connection between Hamilton Berge 1-factorisations of  and Häggkvist's conjecture on Hamilton cycles in 2-connected -regular bipartite graphs, leading us to conjecture that all 1-factorisations of  are Hamilton Berge 1-factorisations.

# Combinatorics of Gene Co-Expression Networks


**Samuel Barton**[1,3]

*Supervisors*: Prof. Diane Donovan[1,3], Associate Prof. Daniel Ortiz-Barrientos[1,2], Dr James Lefevre[1,3]

[1]School of Mathematics and Physics, The University of Queensland

[2]School of Biological Sciences, The University of Queensland

[3]ARC Centre of Excellence for Plant Success in Nature and Agriculture


## Introduction:

### Overview

- **Project Aim** : apply and study *combinatorial structures and techniques* to pure and applied problems in a *quantitative genetics* setting
- **Quantitative Genetics** : is the study of how *gene expression* behaviour and interaction influence genetic variation
- **Gene Expression** : the numerical value counting the abundance of RNA produced by the gene

### Data

- **Purpose** : to study gene behaviour and interactions over time
- **Data Matrix** : rows represent genes, columns indicate time point ratios where the ratios are with respect to the expression of the first time point

## Toy Example:

We now introduce a small synthetic data matrix ($\boldsymbol{M}$) which will be used to show construction and analysis techniques. The synthetic data matrix will be the following:

- **Rows** : represent genes $(g_1, g_2, \ldots, g_{10})$
- **Columns** : time point ratios with $r_1$ being the ratio of gene expression at the second time point compared to the first, $r_2$ is the ratio of gene expression from the third time point to the first, and so on

### Data Matrix Example

$$\boldsymbol{M} = \begin{array}{c} \\ g_1 \\ g_2 \\ g_3 \\ g_4 \\ g_5 \\ g_6 \\ g_7 \\ g_8 \\ g_9 \\ g_{10} \end{array} \begin{array}{c} \begin{array}{cccc} r_1 & r_2 & r_3 & r_4 \end{array} \\ \begin{pmatrix} 2.0 & 2.8 & 3.3 & 1.9 \\ 1.7 & 2.4 & 1.2 & 2.7 \\ 3.9 & 1.3 & 2.2 & 3.9 \\ 3.2 & 3.7 & 3.9 & 1.3 \\ 1.9 & 0.4 & 2.2 & 3.3 \\ 3.5 & 2.9 & 1.3 & 2.9 \\ 0.5 & 2.5 & 2.4 & 3.8 \\ 1.5 & 3.3 & 1.4 & 0.1 \\ 3.7 & 1.5 & 3.0 & 1.4 \\ 3.6 & 2.9 & 1.6 & 2.6 \end{pmatrix} \end{array}$$

For example, for $g_2$ the ratio of gene expression from the first time point to the second is $1.7$.

## Graph Theory Analysis:

### Gene Co-Expression Network

A *gene co-expression network* (GCN) is a graph where the vertex set contains genes and edges represent significant gene co-expression. However, finding significantly co-expressed genes is a complex problem, since there is no single definition for significant co-expression. A common construction technique is described below.

### Gene Expression Profile

For a given gene, the corresponding row of the data matrix is the *expression profile* for that gene. For the toy example, gene $i$ has expression profile:

$$\Big(M(i,1), M(i,2), M(i,3)), M(i,4)\Big).$$

## Graph Theory Analysis:

### Gene Co-Expression Network : Construction

- consider particular gene set
- let each gene be represented by expression profile
- **Vertex Set** : gene set
- **Edge Weight** : absolute correlation between gene expression profiles

We complete this construction for $\boldsymbol{M}$, as seen in Figure 1.

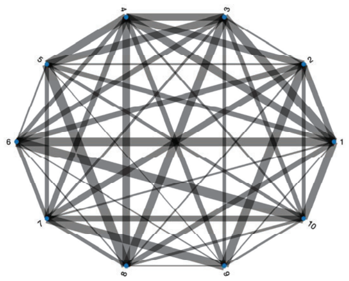

*Figure 1 : GCN for $\boldsymbol{M}$, vertices are genes and edge thickness corresponds to absolute correlation between genes.*

### Analysis Techniques

- this construction technique creates complete weighted graphs
- all possible pairwise relationships between genes are included, creating a dense and complex graph
- **Question** : which pairwise relationships are significant?
- **Solution** : studying the backbone of the graph provides a more useful framework

### Graph Backbone

A *backbone* of a graph is an algorithm which removes edges from a complex graph which are not significant. There are numerous backbone techniques, all of which provide a different definition for a significant edge. One of the most general and well-known is the *Disparity Filter*.

### Disparity Filter

- every vertex generates a threshold score for each incident edge based on vertex strength
- the threshold score for edge $(v, u)$ with weight $w_{v,u}$ from vertex $v$ is:

$$\tau\Big(v, (v,u)\Big) = \left(1 - \frac{w_{v,u}}{\sum_{x \in N(v)} w_{v,x}}\right)^{\left(|N(v)|-1\right)}$$

where $N(v)$ is the set of adjacent vertices of $v$

- each edge will receive two threshold scores
- an edge is removed if both threshold scores are above some selected limit

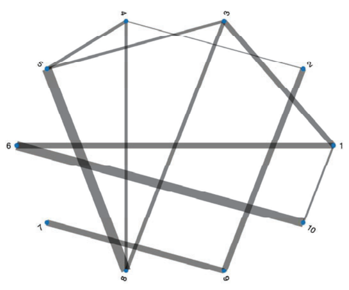

*Figure 2 : backbone of $\boldsymbol{M}$ GCN using the Disparity Filter with threshold limit of $0.02$ (all edges with both threshold scores above $0.2$ are deleted).*

## Graph Theory Analysis:

### Betweenness Centrality

- after applying a backbone, classic techniques (e.g. clustering centrality measures) can be used to study vertex/gene behaviour
- the betweenness centrality is a useful measure based on shortest paths
- the betweenness centrality score ($\beta$) of vertex $v$ is the ratio between the number of shortest paths which include $v$ ($\delta_v(u,w)$) and the total number of shortest paths ($\delta(u,w)$), summed over all pairs of vertices:

$$\beta(v) = \sum_{\substack{u \neq v \neq w \\ u,v,w \in V(\mathcal{G})}} \frac{\delta_v(u,w)}{\delta(u,w)}$$

- for the toy example, the genes each have the following betweenness centrality scores:

$$\begin{array}{cccccccccc} g_1 & g_2 & g_3 & g_4 & g_5 & g_6 & g_7 & g_8 & g_9 & g_{10} \\ (14 & 14 & 18 & 18 & 8 & 0 & 0 & 8 & 8 & 0\,) \end{array}$$

- this suggests that genes $g_1, g_2, g_3, g_4$ play a vital role in this GCN

## Hypergraph Theory Analysis:

### Hypergraph Introduction

A *hypergraph* is the generalisation of a graph, where edges can link more than two vertices. This provides a framework for analysing multi-way relationships. This is particularly useful for gene co-expression, as genes influence many other genes and thus create many multi-way interactions.

### Hypergraph : Construction

- consider particular gene set
- **Vertex Set** : set of time point ratios
- **Edge Set** : gene set
- a vertex (time point ratio) is contained within an edge (gene) when the gene exhibits a $2$-fold change at that time point ratio

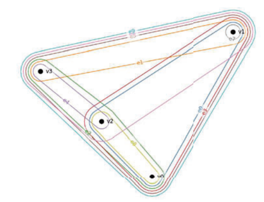

*Figure 3 : hypergraph of $\boldsymbol{M}$, vertices are $2$-fold time point ratios and edges corresponds to genes.*

## Conclusion and Future Directions:

It is clear that graphs only model pairwise interactions, while hypergraphs provide a framework where multi-way interactions can be studied. As such, the future direction of the project is study hypergraph structures and explore the analogous definitions from graph theory such as centrality measures and backbones.

**Title:** Combinatorics of Gene Co-Expression Networks
**Candidate:** Samuel Barton

**Abstract:**
Gene co-expression networks are weighted graphs where vertices represent genes and edges represent significant gene co-expression, weighted with some metric. However, in order to construct these graphs, we require a definition for a significant expression pattern between genes. This definition is dependent on the metric which is used to measure co-expression. As such, different metrics provide different graphs, which in turn highlights different interactions between genes. With most experimental data providing a large number of genes across a small number of time points, the resulting graph is often large and complex. Therefore, it is important to explore various techniques which can be used to filter edges and identify important genes and gene interactions. Since graphs can only model pairwise relationships, while genes often have multi-way interactions, hypergraphs can provide a more useful framework for modelling gene interactions.